

RESEARCH ARTICLE

10.1002/2017JD027445

Key Points:

- Precipitation forecasts are produced at a 4 km convection-permitting resolution over China in summer of 2013–2014
- The 4 km forecast outperforms global forecasts in terms of spatial distribution, intensity, timing, and duration of heavy precipitation
- The unique intraseasonal movement, diurnal cycles, and propagation of summer precipitation in China are also well forecast

Correspondence to:

M. Xue,
mxue@ou.edu

Citation:

Zhu, K., Xue, M., Zhou, B., Zhao, K., Sun, Z., Fu, P., ... Meng, Q. (2018). Evaluation of real-time convection-permitting precipitation forecasts in China during the 2013–2014 summer season. *Journal of Geophysical Research: Atmospheres*, 123, 1037–1064. <https://doi.org/10.1002/2017JD027445>

Received 14 JUL 2017

Accepted 19 DEC 2017

Accepted article online 27 DEC 2017

Published online 17 JAN 2018

Evaluation of Real-Time Convection-Permitting Precipitation Forecasts in China During the 2013–2014 Summer Season

Kefeng Zhu¹ , Ming Xue^{1,2} , Bowen Zhou¹ , Kun Zhao¹ , Zhengqi Sun¹, Peiling Fu¹, Yongguang Zheng³ , Xiaoling Zhang³, and Qingtao Meng³

¹Key Laboratory of Mesoscale Severe Weather, Ministry of Education and School of Atmospheric Sciences, Nanjing University, Nanjing, China, ²Center for Analysis and Prediction of Storms and School of Meteorology, University of Oklahoma, Norman, OK, USA, ³National Meteorological Center, Chinese Meteorological Administration, Beijing, China

Abstract Forecasts at a 4 km convection-permitting resolution over China during the summer season have been produced with the Weather Research and Forecasting model at Nanjing University since 2013. Precipitation forecasts from 2013 to 2014 are evaluated with dense rain gauge observations and compared with operational global model forecasts. Overall, the 4 km forecasts show very good agreement with observations over most parts of China, outperforming global forecasts in terms of spatial distribution, intensity, and diurnal variation. Quantitative evaluations with the Gilbert skill score further confirm the better performance of the 4 km forecasts over global forecasts for heavy precipitation, especially for the thresholds of 100 and 150 mm d⁻¹. Besides bulk characteristics, the representations of some unique features of summer precipitation in China under the influence of the East Asian summer monsoon are further evaluated. These include the northward progression and southward retreat of the main rainband through the summer season, the diurnal variations of precipitation, and the meridional and zonal propagation of precipitation episodes associated with background synoptic flow and the embedded mesoscale convective systems. The 4 km forecast is able to faithfully reproduce most of the features while overprediction of afternoon convection near the southern China coast is found to be a main deficiency that requires further investigations.

1. Introduction

The horizontal grid spacing of numerical weather prediction (NWP) models has been steadily decreasing from hundreds of kilometers in the 1950s (Bolin, 1956; Shuman, 1957) to $O(10)$ km or less (Sun et al., 2013) while the number of vertical levels has increased by an order of magnitude. With rapid development of computational technology, national meteorological services including the National Centers for Environmental Predictions (NCEP) of the United States (Benjamin et al., 2016; Smith et al., 2008), Japanese Meteorological Agency (JMA) (Saito et al., 2006), the UK Met Office (Staniforth & Wood, 2008; Tang et al., 2013), Deutscher Wetterdienst (German Weather Services) (Baldauf et al., 2011), and Météo-France (Seity et al., 2011) have already been operating convective-scale models with horizontal grid spacings ranging from 2 to 4 km, producing forecasts at least twice daily.

One major advantage of NWP models with ~2–4 km grid spacings is their ability to permit, to some extent, explicit representation of cumulus convection (hence the name convection-permitting). At coarser resolutions (~10 km), the representation of convection relies largely on cumulus parameterization, which have deficiencies in representing convective initiation and organization (Liu et al., 2006), propagation (Davis et al., 2003), and diurnal cycles (Clark et al., 2009). In contrast, when convection is explicitly represented on a 2–4 km grid, forecasts of the mode, intensity, and diurnal cycles generally improve (Clark et al., 2007; Fowle & Roebber, 2003; Weisman et al., 2008).

Owing to large domain size and limitation of computing resources, the China Meteorological Administration (CMA)'s operational regional NWP model covering full continental China used a 15 km grid spacing until 2014 when the grid spacing was reduced to 10 km. As part of a national research project to improve the understanding and prediction of convective-scale weather of China (Xue, 2016), and to increase the collaborations between the operational and research communities, a research group at Nanjing University (NJU), China, started to produce experimental 48 h real-time forecasts at a 4 km grid spacing over China twice daily (launched at 00 and 12 UTC) for the summer seasons (from June to August) since 2013. The forecast

products were sent directly to the National Meteorological Center of CMA for experimental use and evaluation. This study performs a systematic evaluation of precipitation forecasts of 2013 and 2014 when the model configurations remained unchanged.

The summer period is selected because it is the main precipitation season with active convective systems in China (Lin & Yang, 2014). Improvements in the summer precipitation forecasts can be invaluable because heavy rainfall is the most serious form of meteorological disaster in China during warm season. According to CMA's yearbook of meteorological disasters (China Meteorological Administration, 2016), financial losses caused by flooding are estimated at 120 billion CNY (~\$18 billion USD) a year.

Summer rainfall in most parts of China is uniquely characterized by its close association with the East Asian Summer Monsoon (EASM). As part of the EASM rainfall, the main precipitation belt in China experiences two abrupt northward jumps as the EASM advances inland from the southern to the northern part of China from late spring through summer. Accordingly, the progression of the rainy season can be divided into three stages (Ding, 1992; Ding & Chan, 2005). The first stage, known as presummer rainy season, begins in April in south China at the onset of EASM and ends in mid-June (Luo et al., 2017). Precipitation at this stage is mostly associated with cold or quasi-stationary fronts. Organized mesoscale convective systems (MCSs) such as squall lines and bow echoes often form along fronts or within the warm sector. The second stage is the so-called "Meiyu" season, which begins around mid-June when the western Pacific subtropical high (WPSH) makes its first jump northward, relocating the major rainband to the midlatitudes. This stage typically lasts for 2 to 4 weeks (Bao et al., 2011). During this period, the cold polar air mass from the north and the warm moisture monsoon air mass from the southern oceans meet at midlatitudes, producing a quasi-stationary west-east oriented rainband extending thousands of kilometers (often from western China through Japan). Persistent precipitation can lead to extreme flooding, causing billions of annual losses.

The third stage begins as the EASM, along with the Meiyu rainband, advances further northward in middle or late July and lasts for about one month. High impact weather events in China often occur during this stage, including the August 1975 Henan "75.8" torrential rainfall (Ding, 2015) and the 21 July 2012 Beijing "7.21" extreme rainfall (Zhu & Xue, 2016). Such heavy precipitation events are often associated with additional synoptic and mesoscale systems such as low-pressure vortices, low-level shear lines, and low-pressure troughs. In some extreme cases, circulations associated with typhoons over the South China Sea can facilitate extreme rainfall through moisture transport (Wen et al., 2015). During the third stage, south China enters its second rainy season as typhoons or other tropical systems become active. In late summer and early fall, the main rainband regresses toward the south as the EASM recedes.

Apart from the spatial distribution of rainfall and its large-scale movement in time, the diurnal cycle is another fundamental characteristic of rainfall and exhibits unique features over China in summer seasons. Owing to its large areal coverage, complex terrain and long coast lines, precipitation diurnal cycles in China exhibit great regional diversity (Yu et al., 2014). In southwest China, especially over the Sichuan Basin (SB; Figure 1a), precipitation generally peaks at midnight. In middle-to-eastern China and south China, dual peaks in early morning and late afternoon are found. The afternoon peak is directly related to local solar heating in most land areas (Dai, 2001) while sea-breeze is also a contributing factor near south China coast (Yu et al., 2008). The mechanisms responsible for the morning peak are more complex, involving possible factors such as the eastward propagating MCSs (Bao et al., 2011), mountain-plain circulations (Sun & Zhang, 2012), diurnal variations of the low-level winds (Chen et al., 2010), and land-sea circulations (Oki & Musiak, 1994).

While the climatological aspects of summer rainfall over China, including the spatial distributions, seasonal movement and diurnal cycles, have been documented through observations (Yu, Zhou, et al., 2007; Zhou et al., 2008) and global model simulations (Yuan et al., 2013), the performance of regional mesoscale models, especially those at convection-permitting resolutions, over contiguous China has not been systematically documented in those aspects. The rainfall characteristics have been used extensively to evaluate both global models (Betts & Jakob, 2002; Dai, 2006; Yuan et al., 2013) and regional models for other regions, especially for the United States (Berenguer et al., 2012; Davis et al., 2003). With improved resolution, the synoptic-scale features of precipitation such as the overall distribution and propagation are generally well predicted (Clark et al., 2007; Weisman et al., 2008). However, difficulties remain in the prediction of meso- β - and meso- γ -scale convection, which can lead to heavy and often localized intense rainfall. The onset time and

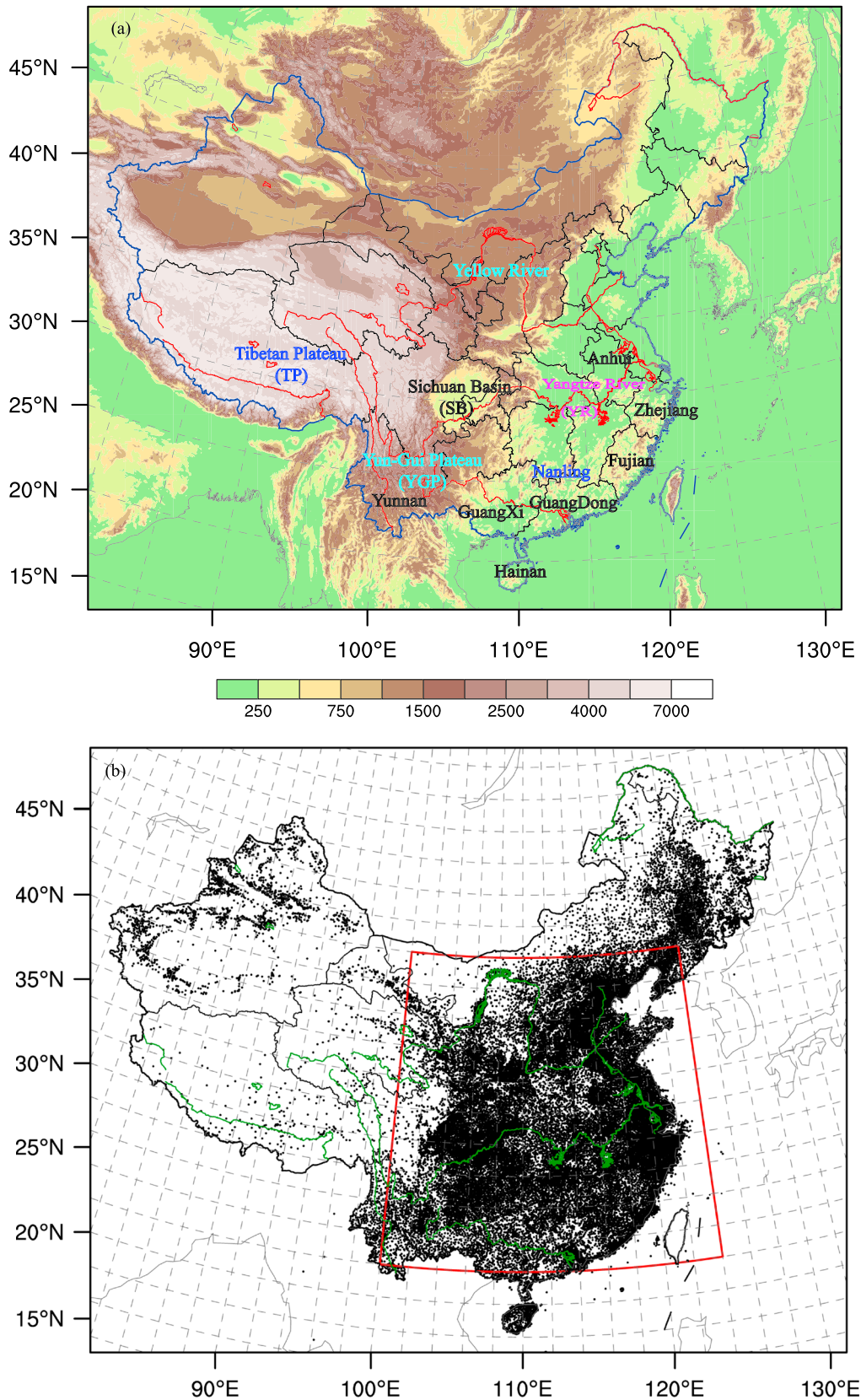


Figure 1. (a) The WRF_NJU forecast domain. The color shading represents terrain height at 500 m intervals. (b) Location of over 30,000 surface stations used in this study. The red rectangle encloses the region where the diurnal cycle of precipitation is calculated.

location, and the development and evolution mechanisms of convection are still not well understood and are often not well predicted even at convection-permitting resolutions (Berenguer et al., 2012).

So far, convection-permitting models, especially the WRF model, have been most extensively evaluated for continental convection over the United States in their storm seasons (e.g., Berenguer et al., 2012; Browning et al., 2007; Weisman et al., 2008) where the synoptic environment is often characterized as being favorable for severe storms. In contrast, the summer months of China are under strong influence of EASM, and the northward migrating Meiyu rainband is a unique, prominent feature. Along the Meiyu front, MCS precipitation tends to dominate while in southern China more disorganized convection is more frequent. Further, over the broad area of China, there are large differences in the precipitation characteristics, some strongly influenced by local terrains, coast lines, and other land surface inhomogeneity. The large-scale synoptic environment over East Asia is also quite different from that of the United States often. For these reasons, the performance of convection-permitting models is likely different, and evaluating and understanding their performance and behaviors are therefore needed.

Therefore, in this study, we evaluate WRF 4 km forecasts against observations with particular emphases on aspects including the spatial distribution, propagation, and diurnal cycles of forecast precipitation, as well as their intraseasonal variations. Quantitative precipitation skills are also examined. To our best knowledge, there is no similar study over China, as existing studies are either limited to one or few case studies, having coarser resolutions, or covering smaller areas or shorter durations.

Another goal of this study is to establish the credibility (as well as identify deficiencies) of the season-long forecast data set so that future studies can be performed using the data set. In addition, systematically documenting the performance of the most widely used WRF model at a convection-permitting resolution in a different climate regime is worthwhile in its own right.

The rest of this paper is organized as follows. Sections 2 and 3, respectively, introduce the configurations of the forecasting system, and the observation data used for verification. Section 4 performs a general evaluation of the precipitation forecasts against observations in reference to operational global model forecasts. Section 5 further examines the monthly mean precipitation, diurnal variations, and propagation characteristics of forecast. Finally, a summary and conclusions are given in section 6.

2. Forecast Configurations

2.1. Configurations of the NJU Real-Time 4 km Forecasting System

The NJU 4 km forecasting system is based on the Advanced Research WRF model (Skamarock et al., 2005) Version 3.3.1 (referred to as WRF_NJU or just WRF hereafter). The forecasts were produced twice daily, starting from NCEP Global Forecasting System (GFS) 0000 and 1200 UTC analyses at 0.5° horizontal resolution, and forced at the lateral boundaries by NCEP GFS real-time forecasts at 3-hourly intervals. The model domain has $1,408 \times 1,080$ horizontal grid points at a 4 km grid spacing with 50 vertical levels (see Figure 1a). Key physics schemes used include the Morrison 2-moment microphysics (Morrison et al., 2005), the Asymmetrical Convective Model version 2 planetary boundary layer scheme (Pleim, 2007), the Pleim-Xiu land surface and surface layer schemes (Pleim, 2006), and the CAM short- and long-wave radiation schemes (Collins et al., 2004). These options were chosen based on extensive tests in the context of multiphysics ensemble using the same model configurations with the 21 July 2012 Beijing "7.21" extreme rainfall event (Zhu & Xue, 2016). The single deterministic forecast used here is also a first step toward storm-scale ensemble forecasts (Xue et al., 2007) that will be able to provide additional probabilistic forecasting information.

2.2. Forecasts From Operational Global Forecast Systems

To demonstrate the advantages of using a convection-permitting resolution for summer precipitation forecasting in China, global forecasts from several operational centers are used as references. They include CMA, NCEP, JMA, and the European Centre for Medium-Range Weather Forecasts (ECMWF). Their products are widely used by Chinese operational forecasters to provide precipitation forecast guidance. The NCEP GFS forecasts at a 0.5° horizontal resolution and 3 h intervals were obtained from the NCEP official ftp site. The rest were retrieved from The Observing system Research and Predictability Experiment Interactive Grand Global Ensemble (TIGGE) archive (Bougeault et al., 2010; Swinbank et al., 2016, available online at <http://apps.ecmwf.int/datasets/>) at a 0.5° horizontal resolution and 6 h intervals.

3. Verification Metrics and Observations

For quantitative precipitation verification, we will use Gilbert skill score (GSS) (Gandin & Murphy, 1992) and frequency bias (FBIAS). To assess the impact of bias on GSS, bias-adjusted GSS is also calculated following Hamill (1999). Rain gauge data from ~30,000 stations are used for verification. Forecast fields are interpolated to the station sites for score calculations in the observation space. Performing the verification at station locations avoids the dependency of the results on the verification grid used although such verifications have their own issues, including the dependency of verification results on the observation network. Additional issues can arise if the network has very disparate density. (We note here that the interpolation from the 4 km grid of forecast precipitation fields to the station sites can be considered an observation sampling process, which effectively filters scales not representable by the observational network. This sampling process is analogous to the actual collection of observations where the observation network samples the continuous precipitation fields. Given the finite resolution of the observational network, aliasing of small-scale structures to resolvable structures can and do occur.)

Specifically, the Model Evaluation Tools (MET) package developed by the Development Testbed Center (Brown et al., 2009) is used to calculate precipitation verification scores in the observation space. For convenience, we first linearly interpolate the global forecast precipitation fields to the 4 km WRF_NJU grid using a utility from the NCEP Unified Post Processor before passing the fields (on the same grid) to MET. Note here that the intermediate interpolation to the 4 km WRF_NJU grid is for convenience only. Direct interpolation from the global fields to the station sites yields very similar results (tested but not shown). For WRF forecasts, we also recalculate the GSS scores by bilinearly interpolating the 4 km WRF precipitation to the 0.5° latitude-longitude grid first. These scores are also included in the score figures and are labeled WRF_NJU_05. The inclusion of the WRF scores from the 0.5° degree grid allows us to assess the potential impact of “double penalty” associated with point-to-point verification of high-resolution fields (e.g., Gilleland, 2013).

The rain gauge measurements used are hourly accumulation data from CMA, and the majority of the ~30,000 stations are automated weather stations. Figure 1b presents the locations of these stations, which are densely distributed in the east and sparsely in the west. The mean separation distance between two adjacent stations in the eastern provinces is about 7 to 8 km. Quality control procedures including removal of duplicate sites, time, and space continuity check and exclusion of abnormal values are performed (e.g., sites far away from the coast reporting more than 1,000 mm d⁻¹ are discarded). The data may still have some quality issues at a few sites, but such issues are limited and should not affect the general results in this paper.

To separate the difference in the GSSs due to precipitation forecast bias, Hamill (1999) computed bias-adjusted GSS by adjusting the precipitation threshold of one model's forecast so that its bias is similar to that of a control forecast. In Hamill's paper, the control forecast's bias happened to be close to 1. Here we choose to use observations as the reference for bias adjustment; i.e., the thresholds for individual models are adjusted so that their biases are all 1. The bias-adjusted GSSs are calculated from a sum of daily contingency tables. Here the statistical significance of GSS is determined by using bootstrap resampling with 3,000 randomly selected times (Candille et al., 2007; Pan et al., 2014). A two-tailed 90% confidence interval from 5% to 95% is calculated.

For subjective evaluations of precipitation in sections 4 and 5, the forecast and observation pairs at observation sites are reanalyzed back to the 4 km WRF grid using a distance-based weighting function with a 24 km influence radius. This way, comparison is only made at locations where there are rain gauge observations. Choosing the verification in the observation space avoids, to some extent, the issue of mismatches between the observation and model resolutions. For the precipitation propagation and diurnal cycle comparisons in section 5, the forecast and observation pairs are reanalyzed to a 0.1° grid (roughly the mean spacing of the rain gauge stations) using Cressman scheme with a influence radius of 0.2°. Due to the latitudinal or longitudinal averaging and/or monthly averaging for the Hovmöller diagrams, very small scale structures are likely filtered out anyway so the smoothing effects associated with the Cressman analysis should be minimal.

4. Verification of Precipitation Forecasts in Comparison to Global Forecasts

In summer, persistent heavy rainfall tends to pose the most severe threat in China by causing flooding. In this section, the WRF_NJU precipitation forecasts at 24 h and 6 h accumulation periods are verified

against observations and compared to several operational global forecasts. Shorter accumulation periods are not available in TIGGE data sets and are therefore not compared. All forecasts evaluated begin at 12 UTC. For spatial distribution figures, forecast period from 12 to 36 h is used to avoid the initial spin-up issue.

4.1. Twenty-Four Hour Accumulated Rainfall

Figure 2a presents observed daily mean precipitation from June through August of 2013 and 2014. The most pronounced feature in the observations is a rainband along the southeast coast that extends from Guangxi to Zhejiang Province (see Figure 1a). Such a pronounced precipitation maximum (Zheng et al., 2016) along the coastline is believed to be forced by convergent onshore flows due to differential friction between the ocean and land (Chen et al., 2014, 2015). Somewhat inland from the coastline in northwestern Guangdong and Guangxi provinces is another region of heavy precipitation, which is associated with orographic lifting by the east-west oriented Nanling Mountain range (Chen et al., 2015). Further west along the southern border of China in Yunnan Province is another line of heavy precipitation that coincides with the southern slope of the Yunnan-Guizhou Plateau (YGP, see Figure 1a). Orographic lifting of the southerly monsoon flow is mostly responsible for the rainfall in this region. In the central part of China, a southwest-northeast oriented rainband is found along the eastern slope of the Tibetan Plateau (TP) and the western edge of the SB. Finally, a east-west oriented rainband due to the persistent Meiyu front is located along the middle and lower reaches of the Yangtze River (YR). A clearer depiction of the Meiyu rainband is presented in Figures 8 and 9 and is discussed later. The overall spatial distributions of precipitation are similar to those found in climatological studies based on longer-period rain gauge measurements (Zheng et al., 2016) and satellite data (Huang et al., 2016).

The 4 km WRF_NJU forecasts (Figure 2b) successfully reproduce the general patterns of precipitation well, including the main regions of heavy precipitation as well as some weaker patches in-between. The predicted intensity is close to the observations except for the southeast coast where precipitation is overpredicted. As will be seen later, most of the overprediction occurs in the afternoon period when disorganized convection is most active, especially near the southern coast where moisture is abundant. There are several possible reasons for such discrepancy. First, overprediction of convective rainfall tends to occur in models using convection-permitting resolutions due to deficiencies in model physics (e.g., Berenguer et al., 2012; Schwartz et al., 2009) and resolution. In idealized squall line simulations, Bryan and Morrison (2011) found that precipitation amount does not converge with resolution until a 250 m grid spacing is used. Also, heavy precipitation along the southern and eastern coastlines is driven by coastal differential friction, land and sea breeze circulations, and thermal and dynamic forcing of coastal mountains and these processes require accurate treatment in the model. Separate studies are needed to identify the true causes for the overprediction.

Precipitation forecasts from global models (Figures 2c–2f) display generally similar spatial patterns as the observations, although detailed features including the shape, intensity, coverage, and position of main precipitation regions vary among models and are less well predicted than in WRF forecasts. For ECMWF (Figure 2c), mean daily precipitation greater than 7.5 mm is predicted over a broader zone near the southern and eastern coastlines. The peak values along the southern coastline are higher than those observed. This is consistent with the study of Kidd et al. (2013), which found that the ECMWF forecasts have wet biases on the landside of the coastal region. In addition, rain intensity and coverage over southern YGP are clearly overpredicted, while the observed rainband west of the SB is underpredicted. The most notable issue with the NCEP GFS forecasts is that the observed precipitation band along the south and southeast coast is mostly missing. Instead, disorganized heaviest precipitation is found over south China in a scattered fashion. The SB rainband is mislocated further south over northern YGP. The JMA forecasts reproduce the coastal rainband well but miss the secondary rain center associated with the Nanling Mountains. The heavy precipitation band to the west of SB is not only mislocated to the south but also misrepresented as a circular zone. The main issue with the CMA forecast is the overprediction of rain intensity and coverage for the coastal rainband and the SB rainband. Note that the CMA model may have large intensity bias in the first 2 days of the forecast but smaller bias in the following 5 days (Swinbank et al., 2016). Overall, WRF_NJU is able to best predict the spatial distributions of heavy and light precipitation among all

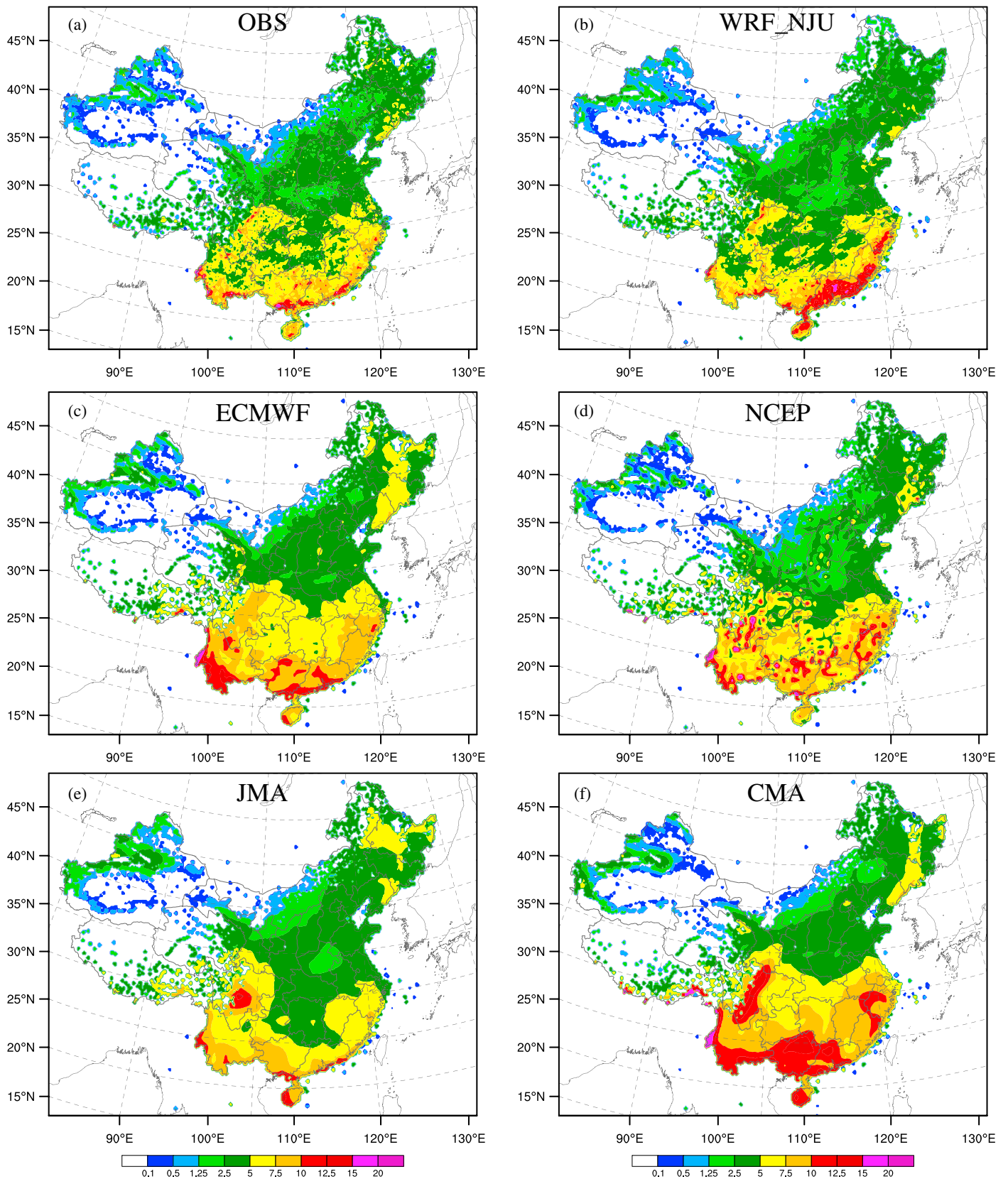


Figure 2. The 24 h accumulated mean precipitation (mm) in June through August of 2013–2014 from (a) rain gauge observations, (b) WRF_NJU forecast, (c) ECMWF, (d) NCEP GFS, (e) JMA, and (f) CMA.

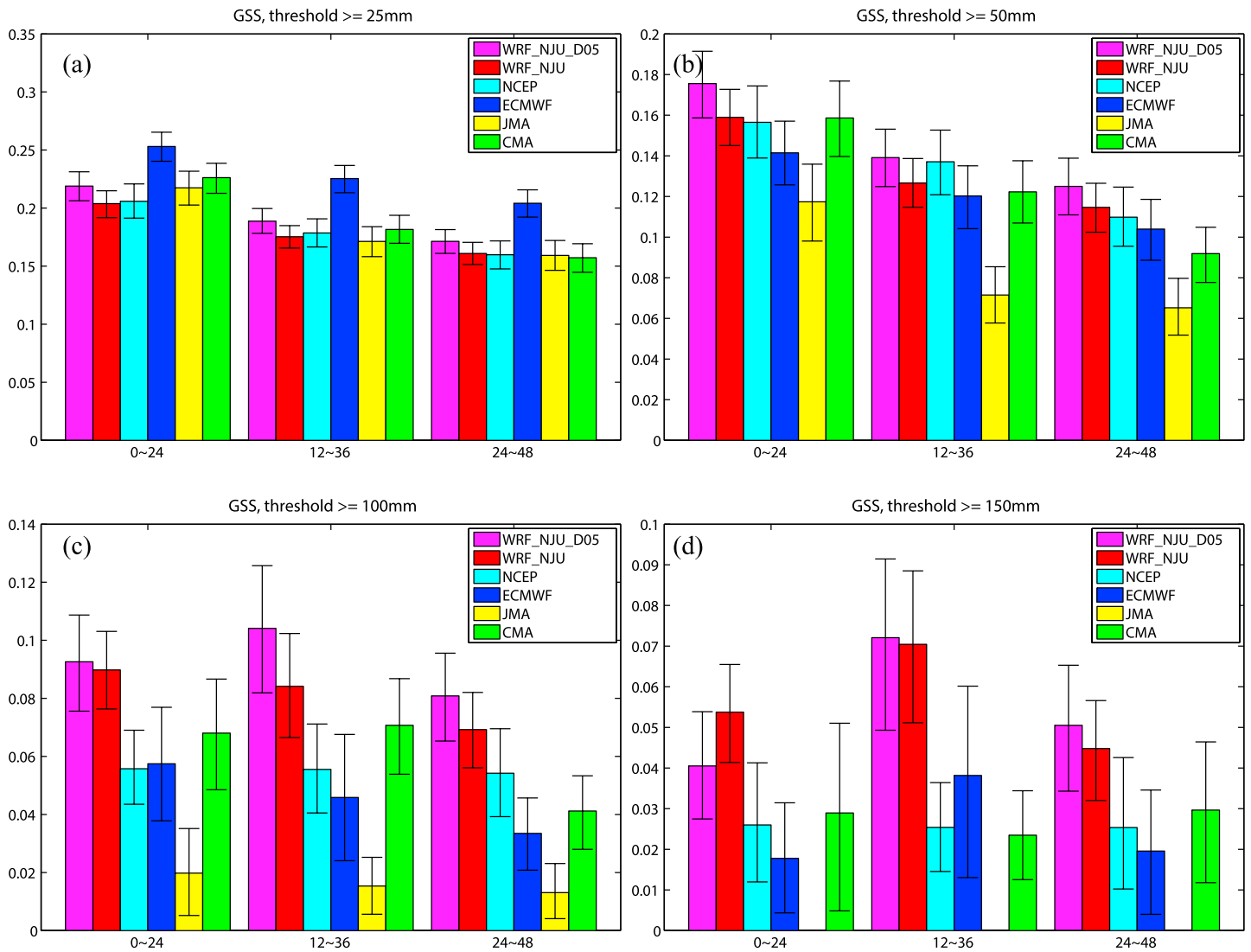


Figure 3. Mean GSS scores of 24 h accumulated rainfall from June to August of 2013–2014 for (a) 25 mm, (b) 50 mm, (c) 100 mm, and (d) 150 mm rainfall. The error bars represent the two-tailed 90% confidence interval: (bottom) 5% and (top) 95%, using the bootstrap distribution method.

models; being able to better resolve geographic features is one of the reasons while explicit handling of convection is another.

To objectively evaluate the forecasts, GSSs are calculated and presented in Figure 3. For the 25 mm d⁻¹ threshold, ECMWF has the highest GSS score (see Figure 3a). The GSSs for other forecasts are comparable. The WRF_NJU forecasts do not show any advantage at this threshold. For the threshold of 50 mm d⁻¹ (heavy rain), WRF performs better, but not significantly better, than global models for the 0–24 h and 24–48 h forecasts (see Figure 3b). The NCEP GFS forecasts have the next highest GSSs while the JMA forecasts have the lowest scores. For 12–36 h forecasts, NCEP GFS is the best. For the thresholds of 100 mm d⁻¹ (very heavy rain) and 150 mm d⁻¹ (extremely heavy rain), WRF forecasts are better than all global models for all forecast ranges, but only significantly better than 2 or 3 global models except for the 24–48 h forecasts at the 150 mm d⁻¹ threshold where only the JMA forecasts are significantly worse. Note that the high GSSs for CMA at 100 mm d⁻¹ apparently benefitted from its large high biases.

The FBIASs of forecasts are presented in Figure 4. For the 25 mm d⁻¹ threshold, the FBIAS of WRF_NJU forecasts is close to 1, indicating no bias or small bias. For higher thresholds at 50 mm d⁻¹ and above (i.e., the heavy rain categories), WRF_NJU tends to overforecast with FBIAS exceeding 1 (Figures 4b–4d). The extent

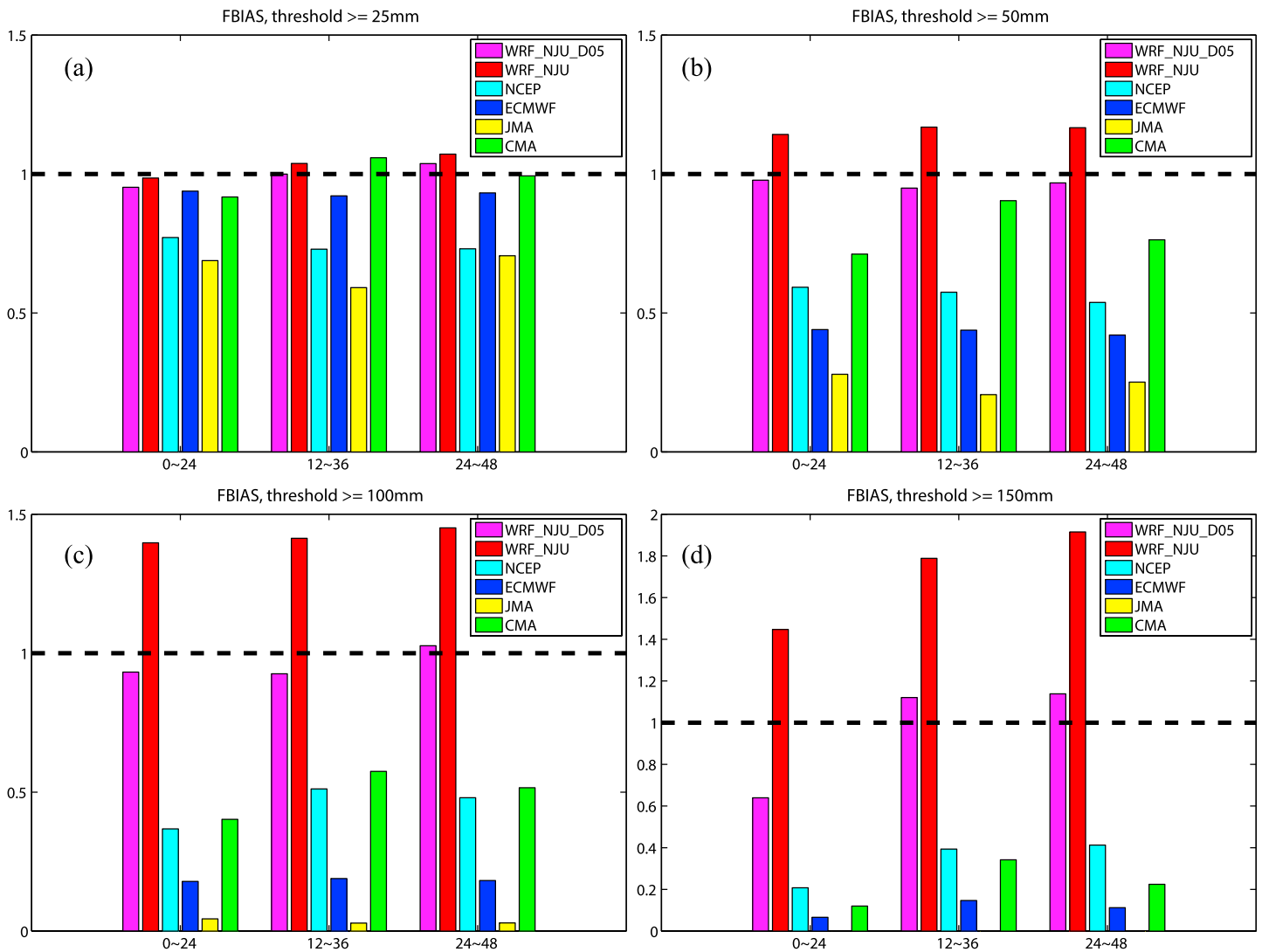


Figure 4. Mean FBIAS scores of 24 h accumulated rainfall from June to August of 2013–2014 for (a) 25 mm, (b) 50 mm, (c) 100 mm, and (d) 150 mm.

of overforecasting also exacerbates with increasing thresholds, approaching 1.5 and 2 for the 100 mm d^{-1} and 150 mm d^{-1} thresholds, respectively. In contrast, the global models exhibit underforecasting for nearly all thresholds (see Figure 4), with the only exception being the CMA 12–36 h forecasts for the 25 mm d^{-1} threshold. This is linked to its overprediction of precipitation area as seen in Figure 2f. The FBIASs for global forecasts generally decrease with increasing thresholds.

For the WRF scores discussed above, the 4 km forecasts were directly interpolated to the observation sites for score calculations. In Figures 3 and 4, WRF scores calculated from forecasts interpolated the 0.5° grid are given as WRF_NJU_05. The GSSs are actually consistently higher than those calculated from the native 4 km fields, except for the 0–24 h forecasts at the 150 mm d^{-1} threshold. Meantime, FBIASs for WRF_NJU_05 are very close to 1 except for the 0–24 h forecasts at the 150 mm threshold. Interpolation to the 0.5° grid acts to smooth out localized heavy precipitation, thereby reducing the positive bias significantly, and the effect is clearly larger for higher precipitation thresholds. With the interpolation, the precipitation fields become smoother and actually reduce the “double penalty” on high-resolution forecasts, leading to higher GSSs. The GSSs of WRF_NJU_05 are higher than those of global models for all forecast periods except for the lowest threshold of 25 mm d^{-1} where ECMWF is still the best. These results also suggest that the use of a high-resolution grid not only allows for the resolution of more structures but also improves the forecast of precipitation structures that are resolvable by coarser-resolution

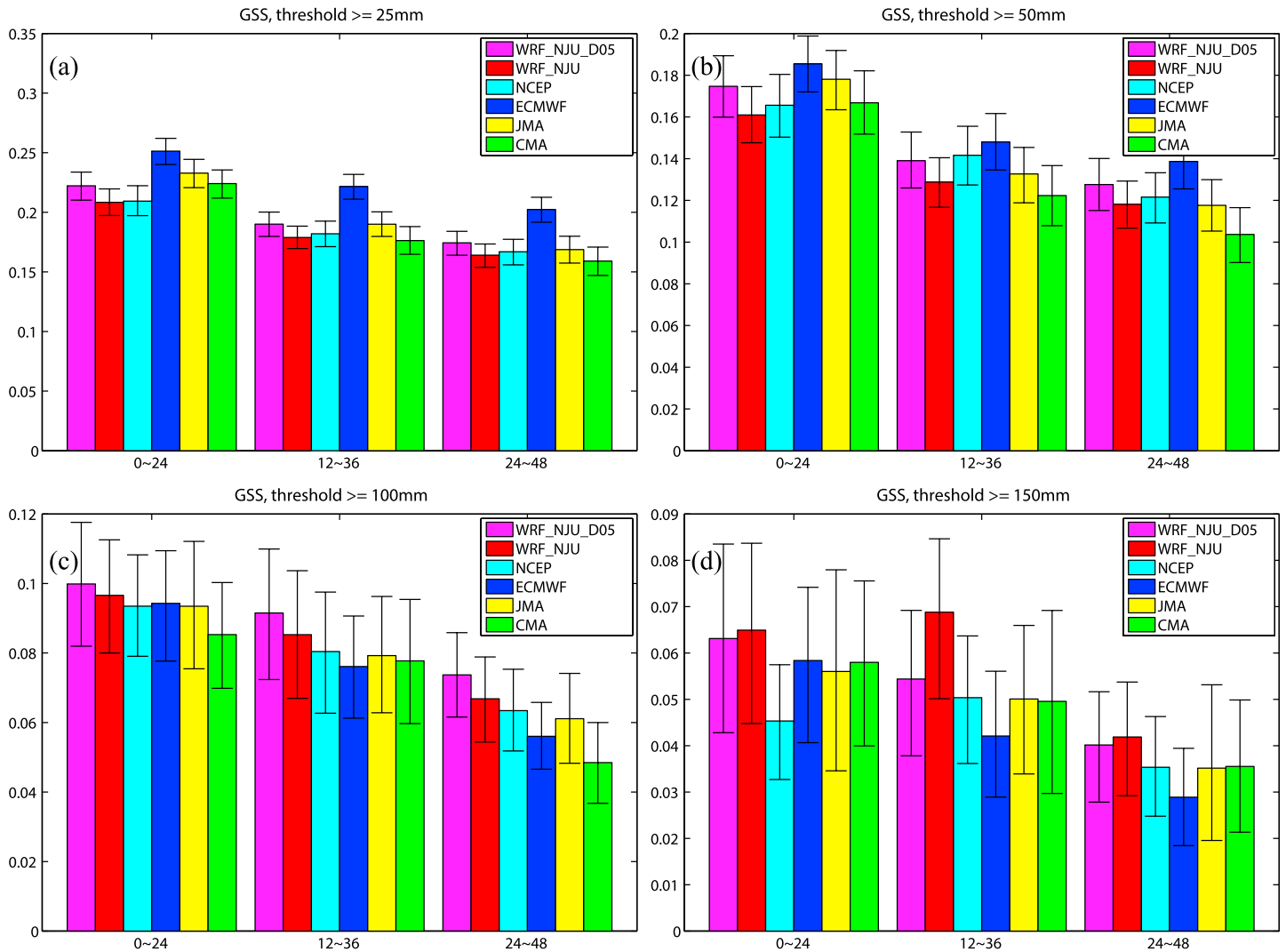


Figure 5. As Figure 3 but for Bias-adjusted GSS scores.

grids. We have also calculated the verification scores of global forecasts directly from their 0.5° grids (without interpolating to the 4 km grid first)—the scores are essentially the same (as expected). Therefore, they are not shown.

The bias-adjusted GSSs based on the idea of Hamill (1999) are presented in Figure 5. With the adjustment, WRF_NJU loses most of its advantage for the 25 and 50 mm d^{-1} thresholds. For the 100 and 150 mm d^{-1} thresholds, the GSSs of WRF_NJU remain the highest among all models but the differences are no longer significant. The relatively high skill of CMA at the 100 mm threshold is also much reduced. WRF_NJU_05 still has higher scores than WRF_NJU for all thresholds except for 150 mm d^{-1} . The bias adjustment increases GSSs overall.

While the bias adjustment exercise is worthwhile, doing it for forecasts with very different capabilities and skills should be viewed with much caution. For a model that can rarely or never forecast extreme precipitation, such a bias adjustment procedure is doing a huge favor for the model. For example, the JMA model rarely forecast 150 mm d^{-1} rainfall (Figure 3), but after adjustment its GSSs are as high and in some cases even higher than other models. This is achieved by reducing the thresholds to very low values. This in a sense introduces a different kind of unfairness. We include the results of bias-adjusted GSSs here for completeness but the results should be viewed with a serious gain of salt. We note here that the global forecasts are included here mainly to provide a frame of reference.

4.2. Six-Hour Accumulated Rainfall

Figure 6 presents the spatial distributions of observed and forecast 6 h rainfall over China, time-averaged over the 2013–2014 summer seasons (note that the TIGGE data are available only at 6 h intervals). As pointed out by many previous studies (Yu, Zhou, et al., 2007; Zhou et al., 2008), different regions of China show different diurnal variations. Nocturnal and morning double peaks occur over most regions of China, while in the SB and along YR, nocturnal peak dominates (Bao et al., 2011; Chen et al., 2009). For the southern coastline and southern YGP, heavy precipitation bands are found in both 08–14 LST (Figure 6a) and 14–20 LST (Figure 6b) periods. For the latter, the south China precipitation band is shifted inland to the Nanling Mountains, mostly due to thermal and dynamical forcing of mountains in the afternoon. For SB, precipitation first occurs on the southeast slope of the basin during 20–02 LST (Figure 6a), and some of it moves off the basin northeastward with prevailing winds during 02–08 LST (Figure 6d). The morning peak is also found along YR especially in its eastern part (Figure 6d), which is mostly related to long-duration Meiyu precipitation (Yu, Xu, et al., 2007). For the rest of China, afternoon peak (14–20 LST) dominates, as can be seen from the heavy rainband near the southern and eastern coasts and relatively (compared with other periods of the day) strong rainfall over northeast China.

Many aspects of the 6 h WRF precipitation forecasts shown in the second row of Figure 6 bear great resemblance to their observed counterparts. They include the width, length, distribution, and the precipitation diurnal variations and propagation. The latter includes the northeastward propagation of the SB rainband from 20–02 LST (Figure 6g) to 02–08 LST (Figure 6h). The biggest issue is the significant over-prediction of afternoon rainfall in south China (Figure 6f) while nocturnal precipitation is much better forecast. Therefore, the overprediction of 24 h rainfall by WRF_NJU (Figure 2b) in this region is mostly due to overprediction of afternoon convective rainfall. Finally, we note that the strong afternoon precipitation maximum over the northern part of the Hainan Island (Figure 6b) is very well reproduced (Figure 6f) and this maximum is strongly influenced by sea breezes, as over the Florida Peninsula (Burpee & Lahiff, 1984).

The overall precipitation patterns from the global forecasts are similar to the observations, although the detailed structures are not as well captured as in WRF_NJU. The NCEP GFS forecasts produce too little rain along the southern coastline (Figure 6i) during the day, and too much rain over the Nanling Mountains and northern YGP in late afternoon and early evening (Figures 6j and 6k). The propagation or diurnal variations of precipitation in the region are not well simulated either. Convection seems to be easily triggered in GFS over northern YGP, especially in the afternoon, and in the meantime shows little propagation after its formation. This is a common problem with coarse-resolution models relying on cumulus parameterization (e.g., Clark et al., 2009). In the ECMWF forecasts, overprediction of rainfall over the northern slope of YGP in the afternoon still exists and covers a broader area than observations (Figures 6m and 6n). The daytime coastal rainfall along the south and southeast coastlines is reproduced, although the spatial extent appears broader than observed. In the evening, the ECMWF forecasts significantly underpredict precipitation over southeast China (Figure 6o), although the nocturnal precipitation along YR is reasonably predicted (Figure 6p).

The most significant issue with JMA forecasts is the overall underprediction of precipitation in all regions, except for the SB where severe overprediction exists at night (Figures 6s and 6t). This result is consistent with the FIAS analysis in section 4.1, where the JMA model gives the lowest values. In the CMA forecasts, afternoon convection over southern China is underpredicted. A precipitation band is predicted in western SB and northern YGP from morning through midnight (08–02 LST; Figures 6u–6w) instead of the observed peak during 02–08 LST (Figure 6d), completely reversing the diurnal cycle of precipitation in the region. In contrast, the morning-to-early afternoon precipitation (08–14 LST; Figure 6u) is significantly overpredicted in southern China in terms of both coverage and magnitude, while the afternoon precipitation (14–20 LST; Figure 6v) is underpredicted. The results suggest that convection in the morning and early afternoon is triggered too early and too easily, leading to too little late afternoon convection. Overall, the diurnal cycles of prediction are handled worst by the CMA global model, while 4 km WRF_NJU handles the diurnal cycles, propagation, and distributions of precipitation best among all models examined.

The GSSs of the 6 h rainfall are presented in Figure 7. For the lowest thresholds of 10 mm, WRF_NJU performs second best behind ECMWF except for the first 6 h, but the differences are insignificant. For thresholds of 15 mm and higher, WRF_NJU performs best except for the first 6 h at 15 mm; it performs significantly

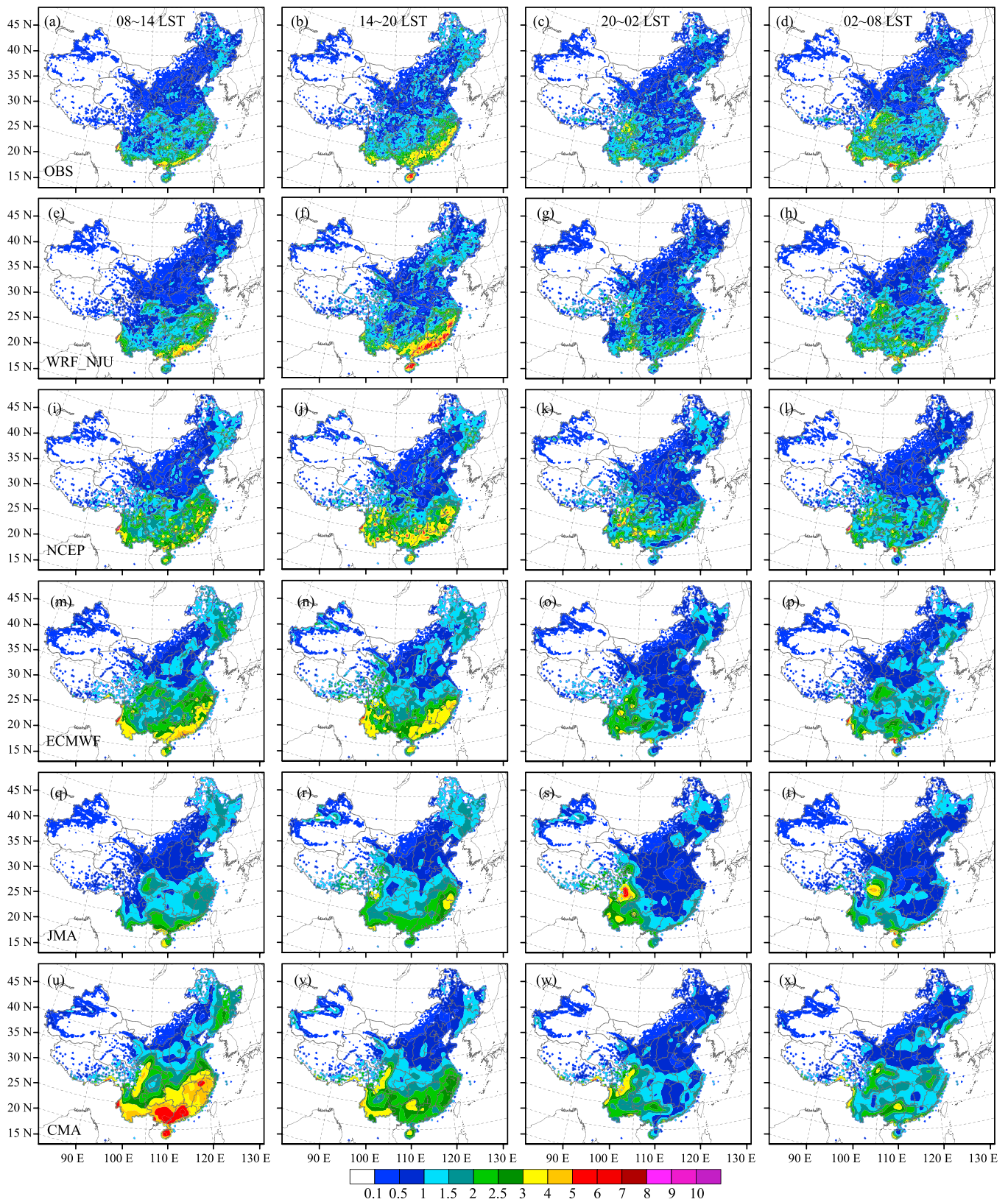


Figure 6. As Figure 2 but for the 6 h accumulated rainfall. (a–d) Rain gauge observations for the four time periods between (a, e, i, m, q, and u) 08–14, (b, f, j, n, r, and v) 14–20, (c, g, k, o, s, and w) 20–02, and (d, h, l, p, t, and x) 02–08 LST. The remaining rows show corresponding forecasts from the WRF_NJU, NCEP GFS, ECMWF, JMA, and CMA models, respectively. The LST is equal to UTC plus 8 h.

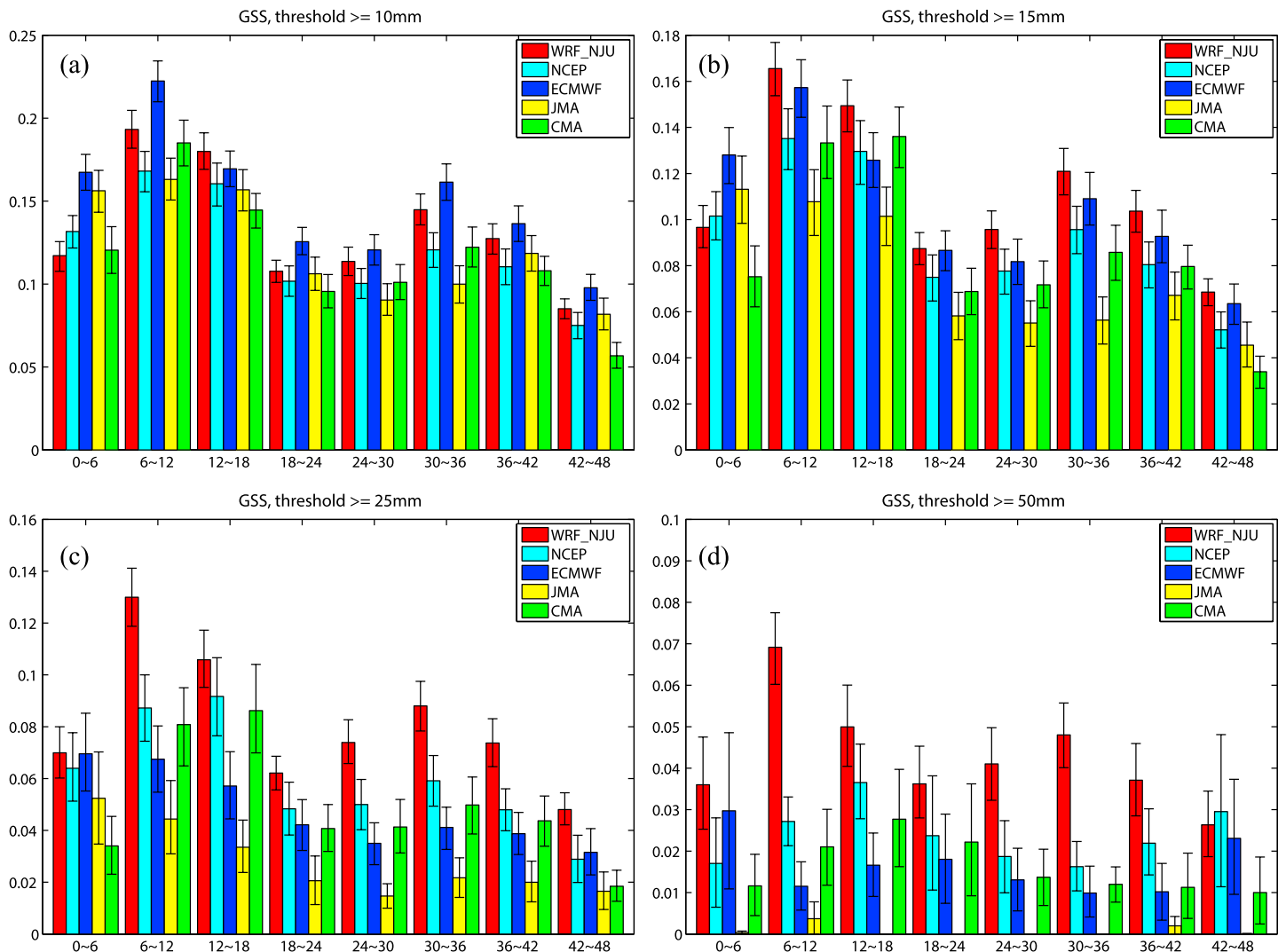


Figure 7. As Figure 3 but for 6 h accumulated rainfall.

better than all other models at the 25 and 50 mm thresholds most times. Compared to 24 h accumulations, WRF's advantages are more clear at the 6 h intervals; this is consistent with its better handling of diurnal cycles and the morning precipitation peak. In fact, the GSSs do also reveal the diurnal cycles, with WRF having the highest scores in the 6–12 h and 30–36 h periods, corresponding to 02–08 LST. The NCEP GSSs show delayed peaks in the scores. Overall, the scores are the lowest in the 18–24 h (14–20 LST) period, suggesting that afternoon convection is the hardest to predict.

5. Further Evaluation of 4 km WRF_NJU Forecasts

Through the verifications against observations in the previous section, the superior performance of the 4 km WRF_NJU precipitation forecasts over four operational global models is established. With that, this section further evaluates the 4 km forecasts with respect to the monthly mean precipitation, diurnal variations, and propagation characteristics that are unique to summer time precipitation in China.

5.1. Monthly Mean Precipitation Spatial Distributions

As described in section 1, summer precipitation over China shows clearly south to north and back to south movements (Ding, 1992). Figure 8 presents the observed and forecast rainfall distributions over the three summer months in 2013 separately. Overall, the spatial distribution and the inner-seasonal movements of rainbands are well forecast.

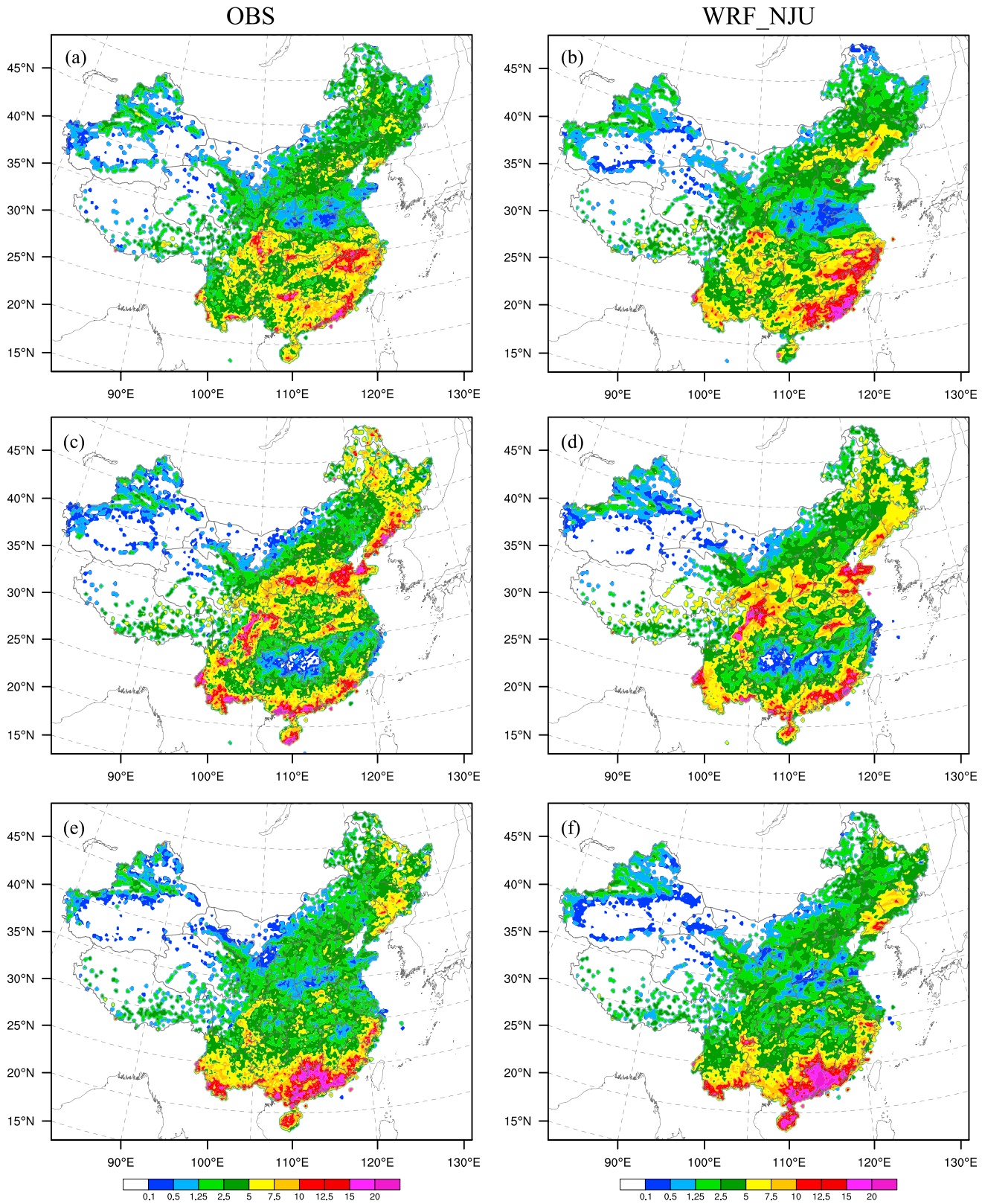


Figure 8. Monthly mean 24 h precipitation of 2013. (a, c, and e) The observed precipitation for June, July, and August, respectively. (b, d, and f) The same as Figures 8a, 8c, and 8e but for WRF_NJU forecast.

The observed precipitation distributions in June 2013 are characterized by two main zones in Figure 8a, one in south China and one along the middle and lower reaches of YR. The first zone is associated with the presummer rainy season when the main precipitation band hovers over south China starting from the onset of EASM in April. Intense precipitation is mainly found along the southeast coastline and around the Nanling Mountain range. Compared to the observations, the WRF_NJU forecasts in Figure 8b capture both intense precipitation regions. However, the spatial extent and intensity of the coastal rainfall is overpredicted, as was also pointed out in section 4. Later this month, a northward jump of the main precipitation band at around 23 June marks the beginning of the 2013 Meiyu season, creating the second precipitation zone along YR in the east part of China (see Figure 8a). The Meiyu rainband is well forecast by WRF_NJU at about the right location and with a similar intensity (Figure 8b). In addition to the Meiyu rainband, the local precipitation center east of TP and west of SB is also taking shape in Figure 8a. The spatial coverage and intensity of the SB rainfall are slightly underpredicted in WRF_NJU.

In July, the main precipitation zone moves further northward to the Yellow River Valley (see Figure 1a for its location) and extends further northeast, following the inland advancement of the EASM (see Figure 8c). In WRF_NJU forecasts, while the location of the north China rainband is mostly in the right place, the intensity is reduced for the northeast branch along the border of China and Korea (Figure 8d). Meanwhile, the northeast-southwest oriented precipitation band around SB becomes fully developed in both observations and forecasts. The coverage of the rainband is somewhat exaggerated toward the northern end in the forecasts. In the south part of China, heavy precipitation continues to be found along the south coast and along the southern edge of YGP. These features are reproduced well in location by WRF_NJU, although differences exist in intensity and coverage south of YGP. Finally, in the central-eastern parts of China around (30°N, 112°E), a local rain center is found in the observations and reproduced by the forecasts. It is associated with orographic lifting of the monsoon flows by the Dabie Mountains in that particular region (Wang et al., 2016).

In August, the intensity of the northern China rainband is greatly reduced, with some precipitation still remaining in the northeast (see Figure 8e) and captured in the forecasts (Figure 8f). Extremely heavy rainfall covers a substantial area over south China, mostly as a result of several landfalling typhoons (see more details in section 5.3). The precipitation forecasts exhibit great resemblance to the observations in these regions, except that the coverage and intensity over Hainan Island are overpredicted, as documented earlier in section 4.2.

The observed monthly mean precipitation in 2014 (Figure 9) appears quite different from that in 2013 (Figure 8). However, upon close examination, the main precipitation zones including the south coast rainband, the Meiyu rainband along YR, and the SB rainband can still be identified, although their onset time, location, intensity, and coverage differ from those in 2013. In June 2014, the coastal precipitation is weaker, while inland precipitation associated with the Nanling Mountains is stronger in south China (Figure 9a). WRF_NJU again overpredicts the strength and spatial extent of coastal rainfall (Figure 9b). Advancing into the Meiyu season (25 June to 18 July), a east-west oriented rainband along YR in central and east China is the most prominent feature of July precipitation in Figure 9c. The EASM did not proceed as far north inland as it did in 2013, so that the northern part of China is mostly free of heavy precipitation. The main Meiyu rainband is well predicted by WRF_NJU (Figure 9d), although the forecast rainband is slightly boarder. The local rainband west of SB is also very well forecast. The August rainfall in south China in 2014 is much more modest compared to 2013, at last partly because no typhoon made landfall that year during this period (Figure 9e). Again, overprediction of convective rainfall along the southeast coast is the major issue found in WRF_NJU forecasts in June and August of 2014 (Figures 9b and 9f).

The annual variations of monthly mean precipitation patterns found in Figure 9 are largely attributed to the positioning of the WPSH. During summer seasons, northward progression and westward extension of the WPSH directly affect low-level moisture transport into China (Lau & Li, 1984; Zhou & Yu, 2005). Figure 10 presents the mean 500 hPa geopotential height overlaid with the 850 hPa horizontal water vapor fluxes for the three summer months. In 2013, the ridge of the WPSH advanced northeastward into China from June onward, reaching north of 30° N in August (Figure 10c). In comparison, the WPSH in 2014 was considerably weaker and was located further offshore. Its ridge remained between 25° N and 30° N in July and August (see Figures 10d and 8f). Related to the retreat of the WPSH was the persistence of a stronger midlatitude East-Asia trough over east China. Associated with such midlevel circulations, the low-level moisture transport

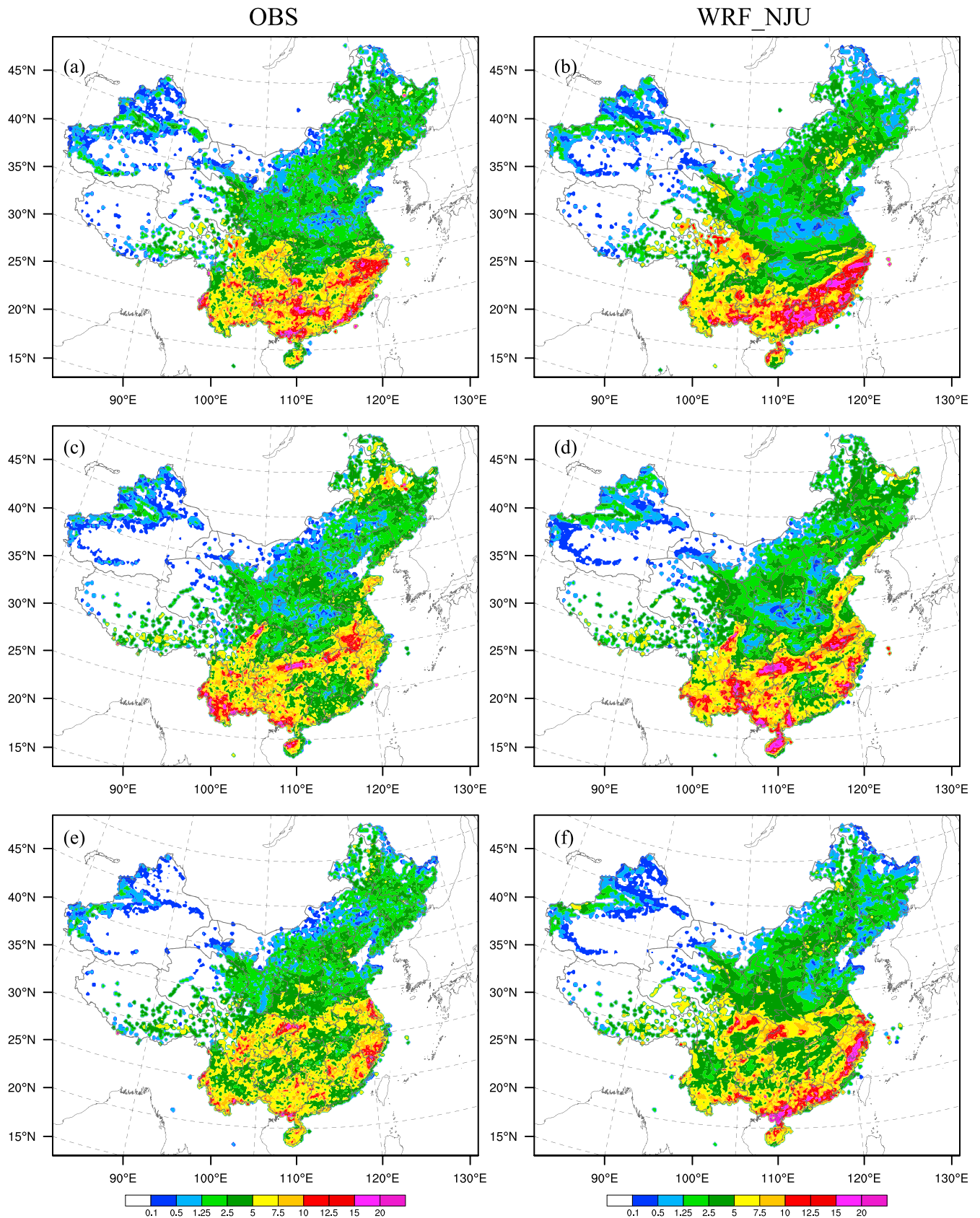


Figure 9. As Figure 8 but for 2014.

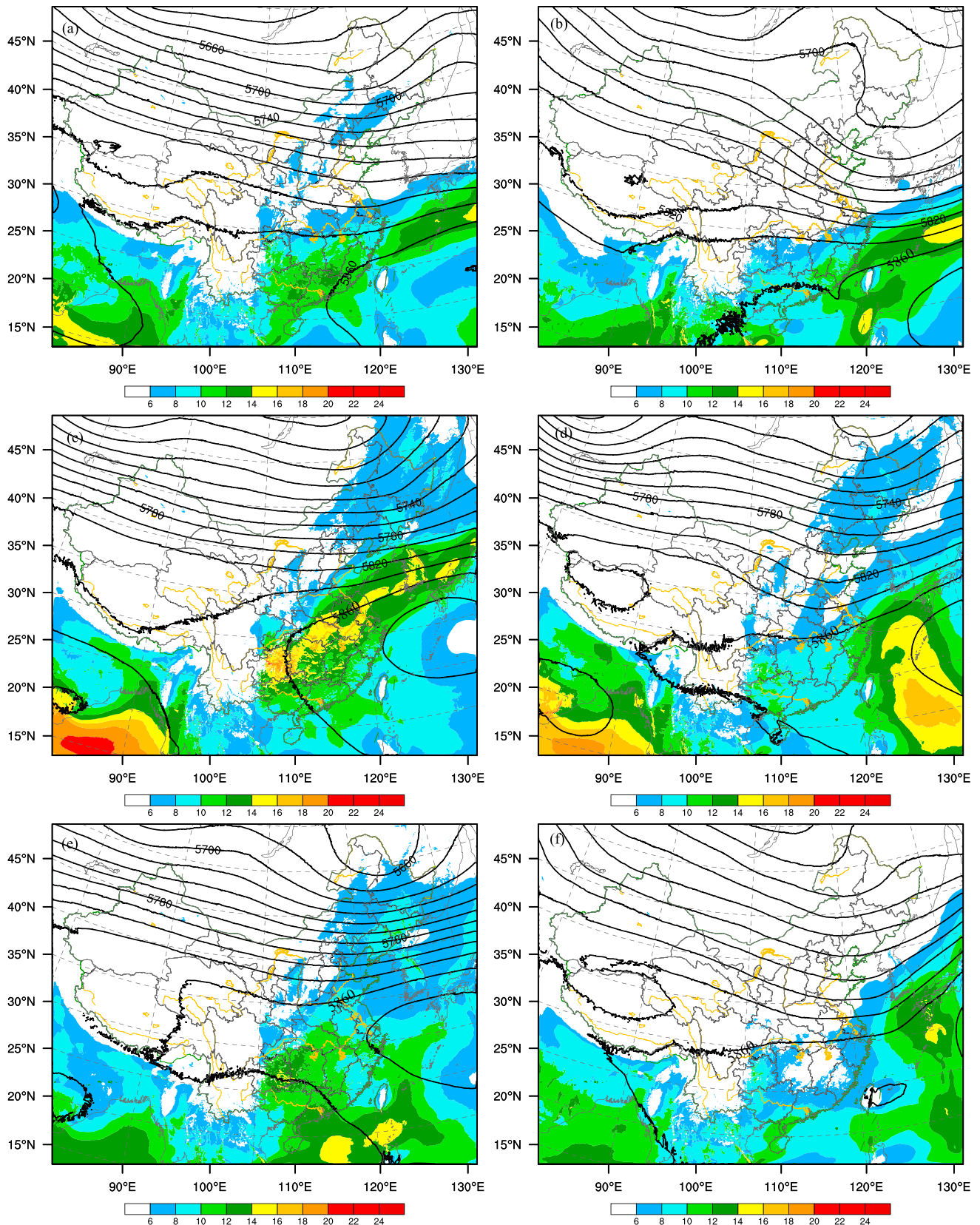


Figure 10. Monthly mean water vapor flux at 850 hPa and geopotential height at 500 hPa. The left and right plots represent year (a, c, and e) 2013 and (b, d, and f) 2014, respectively. The top, middle, and bottom plots are for (a and b) June, (c and d) July, and (e and f) August.

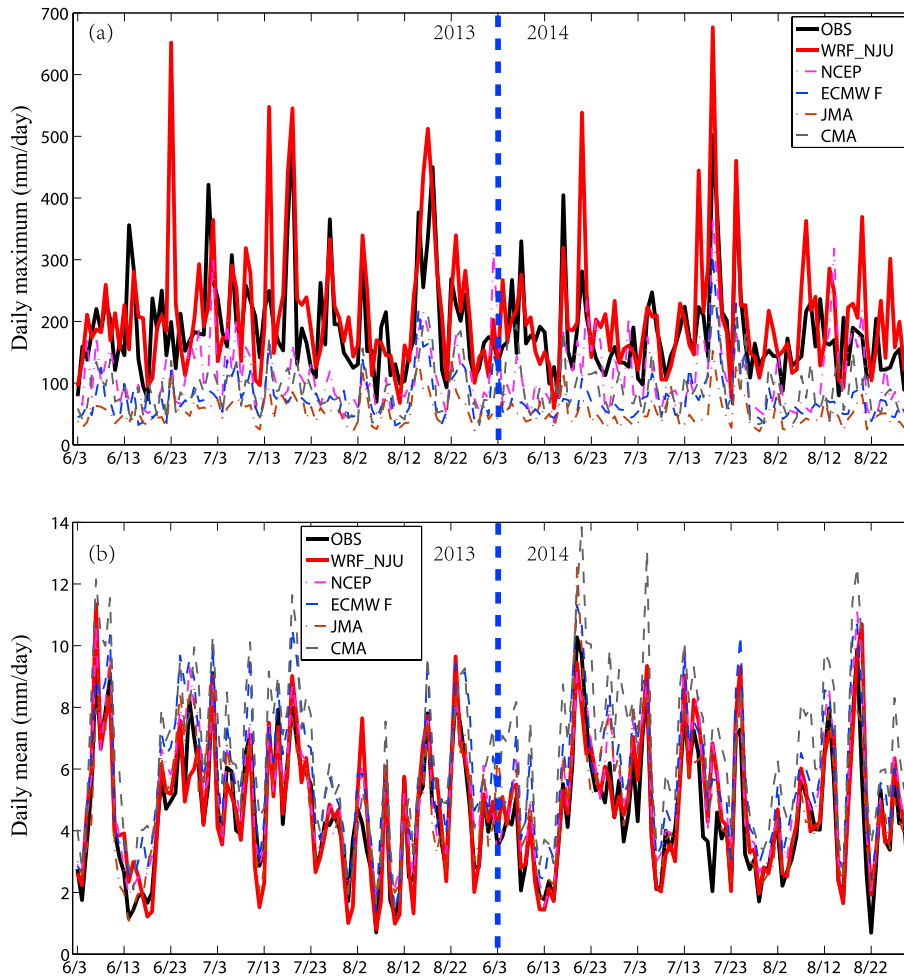


Figure 11. Daily maximum, and (b) daily mean rainfall (mm d^{-1}) from 3 June to 31 August of years 2013–2014. The black thick lines represent observations, and the red thick lines represent the 12–36 h WRF_NJU forecasts starting at 12 UTC. Other thin dashed lines are corresponding global forecasts. The blue dashed lines separate data from year 2013 to 2014. The correlations between observations and forecasts of daily maximum are 0.66, 0.40, 0.56, 0.60, and 0.52 for WRF_NJU, NCEP GFS, ECMWF, JMA, and CMA, respectively, and those for daily mean rainfalls are 0.90, 0.93, 0.94, 0.90, and 0.91, respectively for the different models.

into China was weaker in 2014 than 2013, and hence unable to penetrate deep into northern China (compare Figure 10c to Figure 10d). This explains why heavy precipitation was found over northern China (see Figure 8b) in July 2013, while for 2014, the main rainband was in the central region of China along YR (Figure 9b). Both patterns are reasonably reproduced by the WRF_NJU forecasts as described before (see Figures 8d and 9d).

5.2. Mean Precipitation Diurnal Variations

In this section, the daily precipitation variation and as well as the precipitation diurnal cycle are further examined. The observed and forecast daily maximum and mean precipitation of WRF and global model forecasts, averaged over all rain gauge stations, for each summer day in 2013–2014 are presented in Figure 11. Overall, the WRF_NJU forecasts closely follow the observations for both daily maximum and mean precipitation while the global models have similar performance for mean precipitation but significantly underpredict the daily maxima. Specifically, WRF_NJU predicts correct daily maximum most times, although overpredictions including a few severe ones do occur from time to time (Figure 11a). This is consistent with Figure 4, where WRF_NJU is found to overpredict heavy rain events ($\geq 50 \text{ mm d}^{-1}$) and most of these extreme amounts were actually associated with landfalling typhoons. The correlations between the observed and forecast time series for daily maximum precipitation are 0.66, 0.40, 0.56, 0.60, and 0.52 for WRF_NJU, NCEP GFS, ECMWF, JMA, and CMA, respectively, with the correlation of WRF_NJU being the highest. Nevertheless, because correlation coefficient does not take into account amplitude error, these numbers do not full reflect the relative quality of forecasts; from Figure 11a, it is clear that the global models seriously underpredict the daily

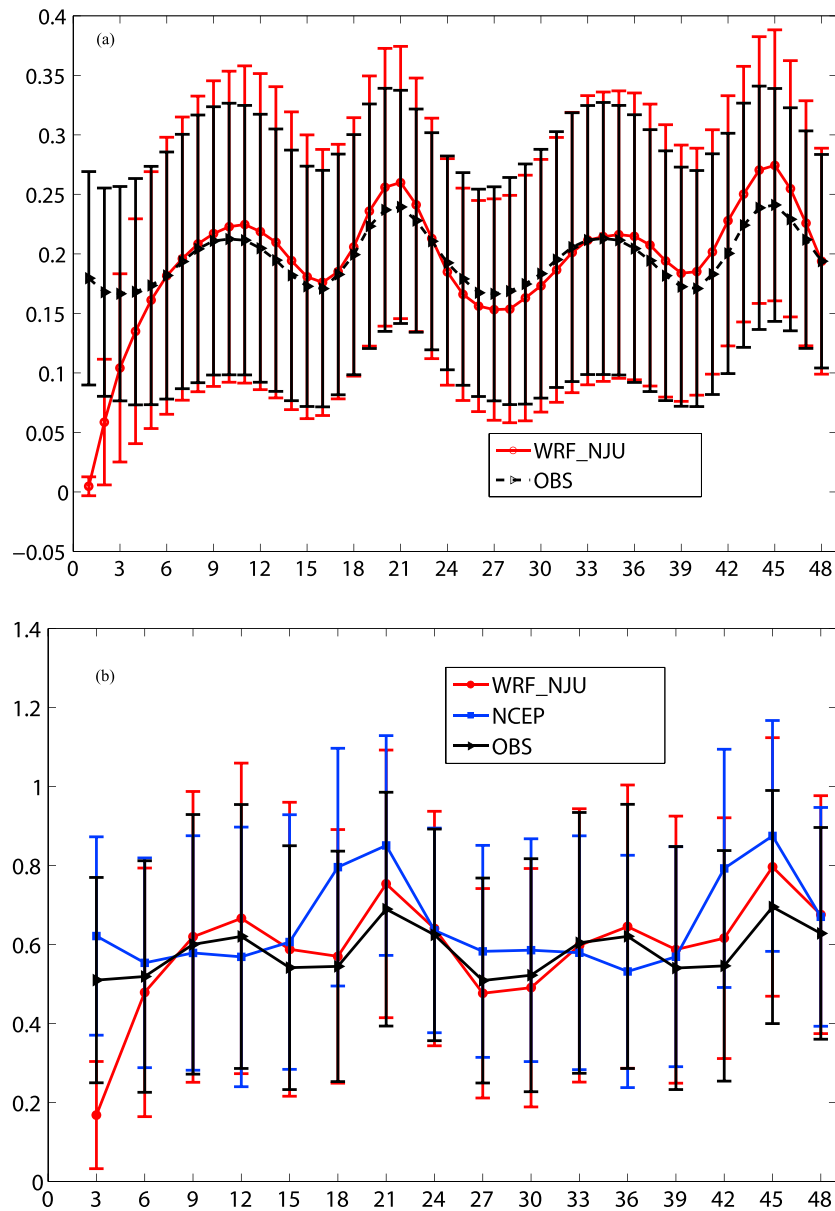


Figure 12. The 48 h time series of observed and forecast starting from (a) 12 UTC hourly rainfall and (b) 3 h accumulated rainfall, averaged over all rain gauge stations for the summer seasons of 2013–2014. The error bars represent one standard deviation of each forecast hour.

extreme rainfall, with JMA being the worse. For daily mean precipitation, all forecasts perform well in terms of the correlation coefficient, given the relatively easy task of getting the day-to-day trend right (Figure 11b). The correlations are 0.90, 0.93, 0.94, 0.91, and 0.91 for WRF_NJU, NCEP GFS, ECMWF, JMA, and CMA, respectively. In terms of the amplitude, CMA has the most serious overprediction (Figure 11b).

The observed and forecast 48 h time series of hourly rainfall, spatially averaged over China and time-averaged for the two summers, are presented in Figure 12a. Forecasts starting from 12 UTC (20 LST) are used for this plot. The underprediction during the first 6 h is due to model spin-up. Time series of the observed hourly rainfall are very well simulated, except for around 21 and 45 h of forecast or 17 LST when slight overprediction occurs. The variances of the hourly rainfall, as represented by the error bars, are also properly forecast, with some overprediction around the same late-afternoon hours when mean values are also overpredicted. In terms of temporal pattern, both observations and forecasts exhibit bimodal structures. The highest peak is found in late afternoon at 21 and 45 h of forecast corresponding to 17 LST. A secondary peak of nearly

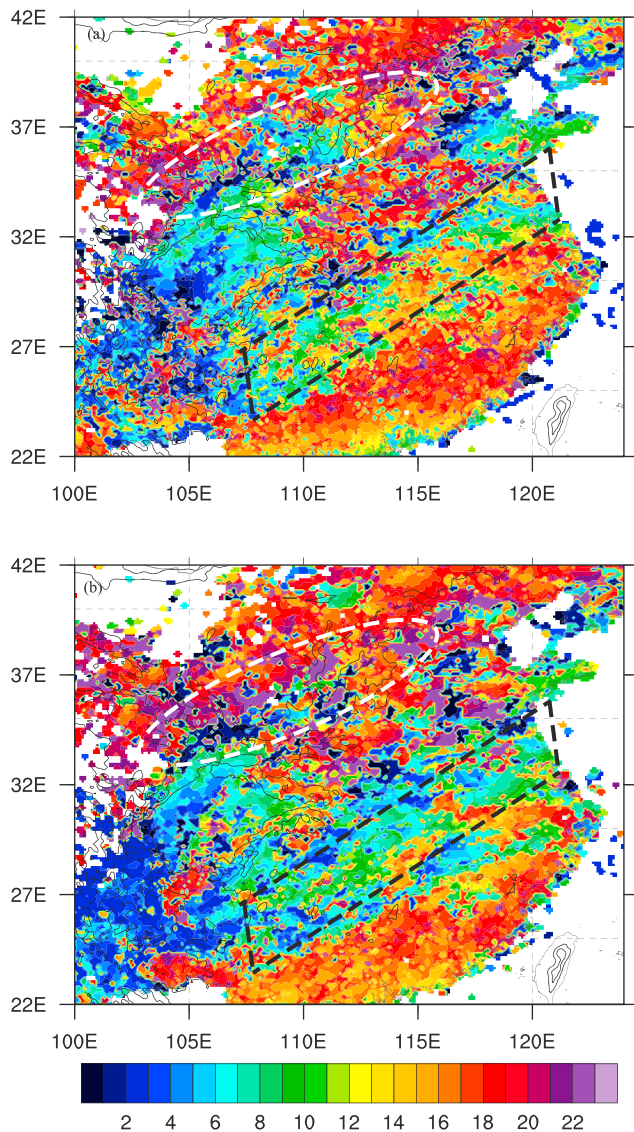


Figure 13. Local solar time (LST) corresponding to the peak diurnal precipitation in the (a) observation and (b) WRF_NJU forecasts. The white ellipses and the black parallelogram highlight regions where major differences exist between observations and forecasts.

comparable magnitude occurs in early morning (06 LST) at 10 and 34 forecast hours. The predicted morning peak has a 1 h delay, to 07 LST. In comparison, the NCEP GFS forecasts fail to reproduce the early morning peaks in both first and second 24 h. For the main afternoon rainfall peak, the NCEP GFS also gives more severe overpredictions than WRF_NJU. The afternoon precipitation also occurs 2–3 h earlier (Figure 12b). The GFS results are consistent with Yuan et al. (2013), who used the Community Atmospheric Model version 5 (CAM5) (Neale et al., 2010) to simulate summer precipitation over China. They found that CAM5 failed to reproduce convective rainfall in the morning over the western and eastern plains of China while stratiform rain for both regions was well simulated.

Following Yuan et al. (2012), color maps of the observed and predicted peak hours of diurnal precipitation of both summers are presented in Figure 13. Results are obtained by first obtaining the peak hour from hourly mean precipitation time series (similar to Figure 12a) at each rain gauge station. The final results are interpolated onto the 4 km model grid for graphic plotting. The observed patterns in Figure 13 are similar to those from Yuan et al. (2012), except that more detailed structures are revealed here due to the use of denser surface observations. Detailed descriptions of the daily peak hours in different regions of China and discussions on their possible causes can be found in Yu, Zhou, et al. (2007) and Chen et al. (2010).

In south China (below the black parallelograms), consistent late afternoon peaks are founded in both observations and forecasts in Figures 13a and 13b. Note that right along the southeast coastline, a narrow strip of morning peaks is observed. This behavior is also reproduced in WRF_NJU. Moving toward the midlatitudes, the forecasts tend to overpredict the area of early morning to noon peaks in regions enclosed by the black parallelograms. This is evident by the presence of more greens and blues within the parallelogram in Figure 13b than those in Figure 13a. The precipitation peaks over YGP (west of black parallelograms) are characterized by mostly midnight to early morning peaks, with scattered late afternoon peaks in rather limited areas (Figure 13a). This region is forecast reasonably well, except that the spatial extent of late afternoon peak (red colors) is a little overpredicted. Over TP (close to 100°E), the forecasts show similar late afternoon and early morning peaks while over the east slope of TP and its adjacent SB, midnight to early morning peaks are correctly simulated. Further north, the majority of precipitation peaks transition from morning toward late afternoon. While the general transition pattern from the forecasts is similar to observations, some observed morning peaks within that region, encircled by the white ellipses, are not well simulated. The spatial coverage of late evening peaks (purple colors) are exaggerated in the forecasts. Finally, in the north-most region of Figure 13, late afternoon peaks dominate over most of the region in both observations and forecasts.

5.3. Precipitation Episodes and Propagation

Precipitation episodes and propagation within a broad region between 22°–42°N and 100°–124°E (see red box in Figure 1b), covering the main summer precipitation regions, are examined with time-space Hovmöller diagrams (Carbone et al., 2002) in Figures 14 and 15. To avoid the spin-up and overlap issues, daily 12–36 h forecasts, starting from 12 UTC, are again used. To aid cross-referencing of the episodes, main precipitation episodes are labeled A through N on the Hovmöller diagrams of observations in Figures 14 and 15.

During the first two weeks of June 2013, or in the presummer rainy season, the main precipitation events occur mostly south of 26°N (see episodes A and C, Figure 14a) with the rain centers located over the

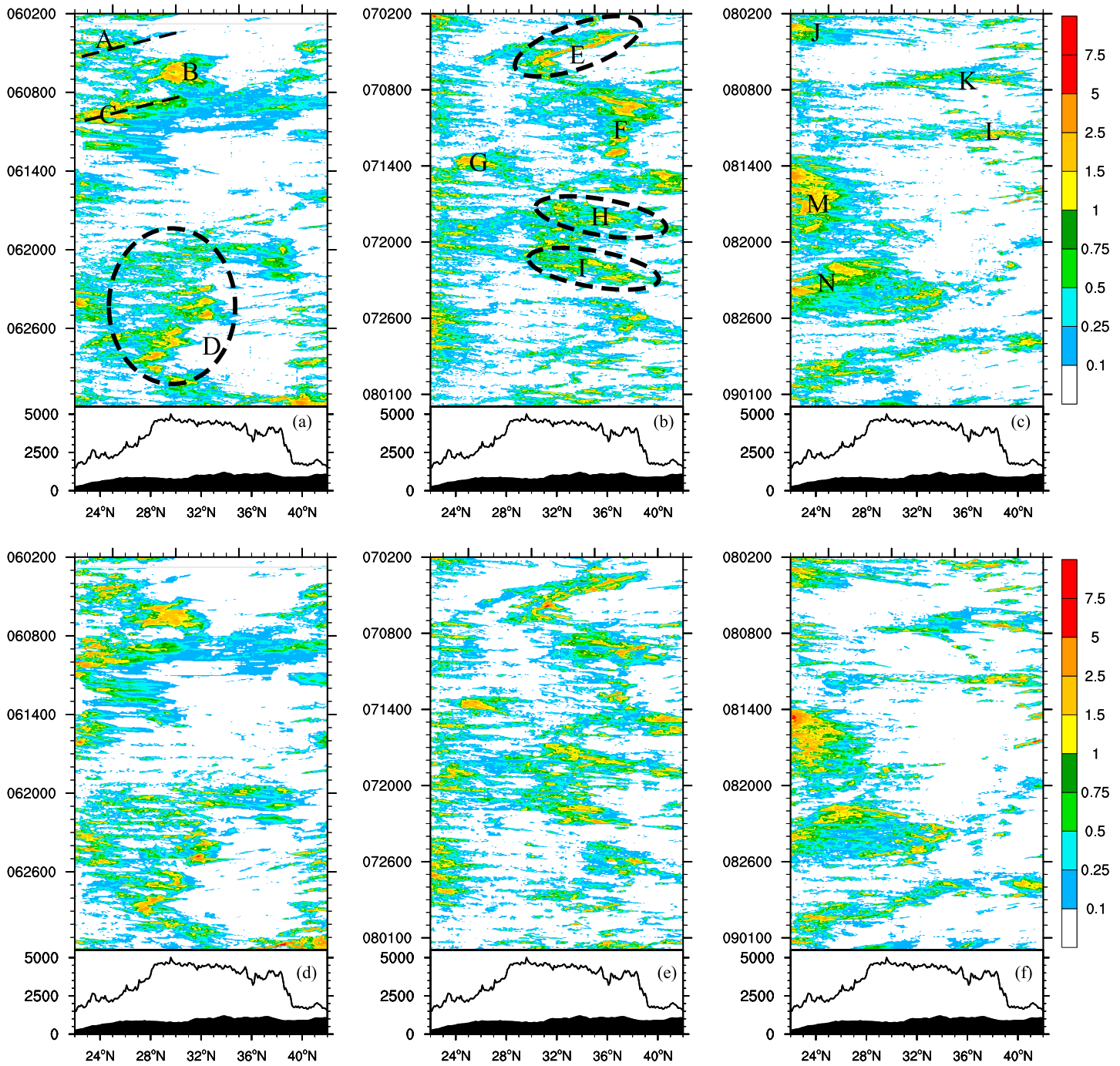


Figure 14. Time-latitude Hovmöller diagrams of rainfall in summer 2013. Rainfall is averaged from 100°E to 124°E within strips of 0.1° latitude width. The top and bottom rows represent rain gauge observations and WRF_NJU forecasts. The columns represent June, July, and August. The curves and shadings below each sub-figure show the maximum and mean terrain heights, respectively. The capital letters in the top row represent individual precipitation episodes.

Nanling Mountains (see also Figure 8a). Both episodes show north to south movements over periods of about 2 days, as marked by the dashed lines in Figure 14a. As China enters the Meiyu season, the main rainband jumps to midlatitudes along YR between 20 June and 8 July. Episodes D and E in Figures 14a and 14b are Meiyu frontal precipitation events that also exhibit southerly propagation characteristics. After that, the main rainband further jumps to ~36°N in northern China and stays there for a month or so, producing rain episodes of F, H, I, K, and L in Figures 14b and 14c. In July and August, four

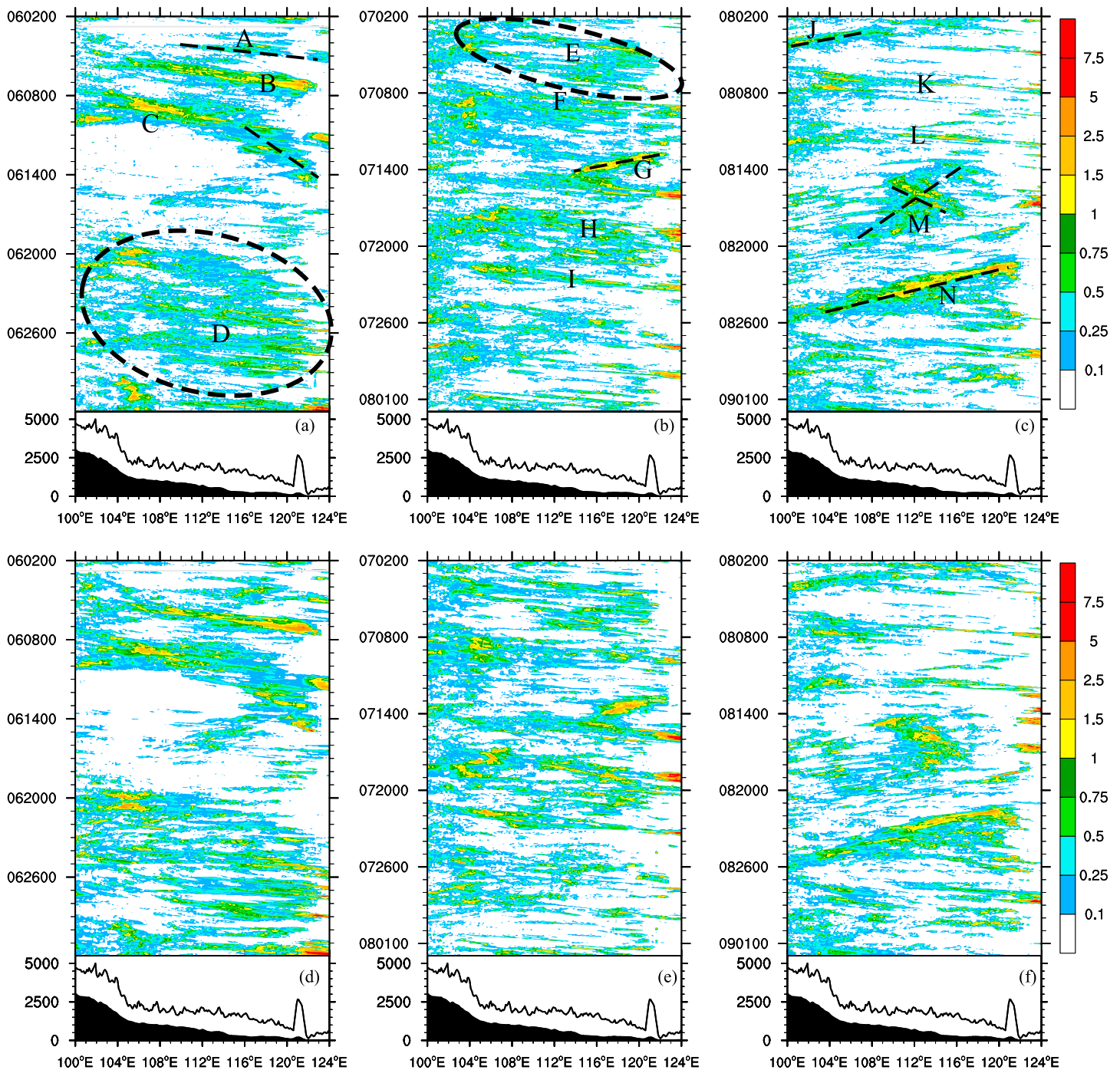


Figure 15. As Figure 12 but for the time-longitude Hovmöller diagrams. Rainfall is averaged from 22°N to 42°N within strips of 0.1° longitude width.

observed precipitation episodes (G, J, M, and N) associated with landfalling typhoons are found at lower latitudes close to the south coast. Usually, they show south to north movements. In general, the WRF_NJU forecasts are able to reproduce the meridional span, the temporal duration, and the propagation characteristics of each of the main precipitation episodes. However, some differences in the intensity and position of precipitation streaks do exist. For example, for episode C, the forecast rainfall is closer to the coastline than that in the observations before mid-June (Figures 14a and 14d). The same location discrepancy is also seen previously in the monthly mean precipitation forecasts (see Figures 8a and 8b).

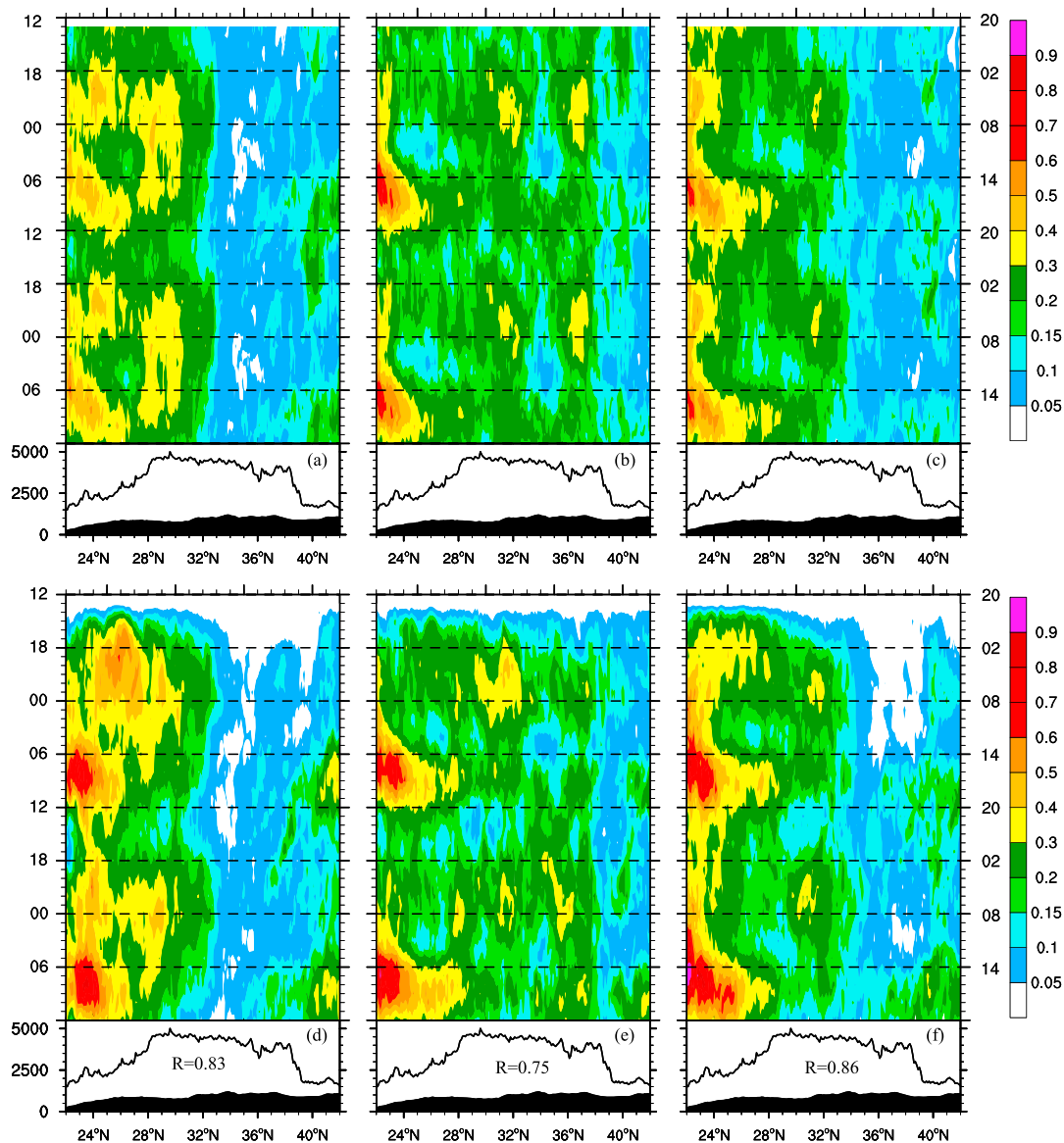


Figure 16. Hovmöller diagrams representing the diurnal cycle of precipitation averaged zonally within strips of 0.1° latitude width between 100°E and 124°E in years 2013–2014. The top and bottom rows represent rain gauge observations and WRF_NJU forecasts. The columns represent June, July, and August. The time axes of left (right) are in UTC (LST). Data from all 48 h of forecast starting at 12 UTC are included. The correlation coefficient (R) of the forecast with its corresponding observation is given in the bottom panels.

While meridional propagation mostly represents synoptic and large-scale system movement, zonal propagation corresponds mainly to the movements of embedded MCSs. Labels A–N in Figure 15 represent the same rainfall systems as those in Figure 14. In the observations, most of the precipitation episodes propagate from west to east (see dashed lines A–E in Figures 15a and 15b). This is due to the prevailing steering-level westerly winds over midlatitudes during the summer. Episodes with the opposite westward propagation are mostly tropical cyclones (G, J, M, and N) that make landfall on the east coast of China. Among them, typhoon M retains strong circulation over land. Rotation of the spiral rainband gives rise to some eastward movement of precipitation. Overall, the WRF_NJU forecasts perform well in replicating the width of precipitation streaks as well as the propagation speed and directions. These are very clearly seen with episodes B, C, D, G, H, I, M, and N. However, as many previous studies (Berenguer et al., 2012; Davis et al., 2003) found, biases in intensity, onset position, and duration of embedded convection are still noticeable, especially in details (see convection ranging from yellow to red colors in Figure 15).

The onset timing and subsequent propagation of precipitation associated with the morning and afternoon periods are well represented in the WRF_NJU forecasts. This is also supported by the high correlation coefficients between forecasts and observations, which are 0.83, 0.75, and 0.86 for June, July, and August, respectively. These values are close to those given in Clark et al. (2009) for 4 km forecasts produced for the late spring season over the United States. However, overprediction of the intensity of afternoon rainfall in south China especially in June (Figure 16d) and August (Figure 16f) again stands out as the major forecast deficiency of WRF_NJU.

In the time-longitude Hovmöller diagrams in Figure 17, the two intense precipitation periods in the morning and afternoon can also be identified. The afternoon peak occurs most evidently between 116°E and 122°E for all three months, and near 100°E over TP and YGP, especially in June (Figure 17a). Agreeing with Bao et al. (2011), there is little east-west propagation of the afternoon peak in either observations or forecasts. Compared to the observations, the afternoon peaks appear stronger in the forecasts. Unlike the stationary afternoon peaks, the early morning peaks show eastward propagation west of 112°E. The maximum morning rainfall is found between 100°E and 103°E. This is mostly contributed by the precipitation over YGP as evidenced in Figure 13. The WRF_NJU forecasts exhibit similar zonal propagation pattern as observations. The correlation coefficients between forecasts and observations are 0.67, 0.57, and 0.56 for June, July, and August, respectively. They are lower than their counterparts in Figure 16, but are still considered modest. As previously mentioned, the zonal propagation mainly reflects the movement of MCSs within the precipitation streaks. Although the convection-permitting model is beginning to resolve convection, its accuracy still limited by the resolution. Therefore, it is not surprising that the correlations for zonal propagation are not as high as those for meridional propagation, a lot of which is associated with movement of synoptic systems.

6. Summary

This study describes experimental 48 h real-time forecasts at a 4 km convection-permitting resolution over entire China. These forecasts were produced at the Nanjing University, China, twice a day using the WRF model (called WRF_NJU here) over the summer seasons starting from 2013, as part of a national research project to improve the understanding and prediction of convective-scale weather of China. This study presents a comprehensive evaluation of the precipitation forecasts of WRF_NJU against a dense network of rain gauge observations. Furthermore, the WRF_NJU forecasts are compared to four operational global models' forecasts to assess the advantages of using a convection-permitting resolution for summer-time precipitation in China. Aspects examined cover not only the spatial distribution, timing and duration, and intensity of rainfall but also the diurnal cycles of precipitation and the propagation characteristics, which are unique to summer season rainfall over China. Main findings are summarized below.

The mean 24 h accumulated precipitation is first examined to evaluate model forecasts. The 4 km WRF_NJU forecasts quite accurately reproduce the spatial extents and orientations of the main regions/bands of heavy precipitation. Those include a distinct narrow zone of rainfall along the south and southeast coastline, a secondary region off the south coast over the Nanling Mountains, a local region along the southern edge of Yunnan-Guizhou Plateau in southwest China, a northeast-southwest oriented line along the western edge of Sichuan Basin, and a west-east oriented band along the Yangtze River associated with the Meiyu frontal system. Compared to the observations, the main deficiency of the WRF_NJU forecasts is the overprediction of intensity and coverage of precipitation near the south and southeast coast. For the global forecasts, the spatial distributions of precipitation centers are less well reproduced. For example, the intensity of the rain-band west of the Sichuan Basin is too weak (intense) in the ECMWF (NCEP GFS) forecasts. Its linear spatial extent appears too board in the CMA forecasts and is misrepresented as a circular region in the JMA forecasts. When quantitatively evaluated against observations, the WRF_NJU forecasts outperform global forecasts for heavy rainfall ($\geq 50 \text{ mm d}^{-1}$) events, though not significantly better. In terms of FBIA, the WRF_NJU biases are closest to unity for the moderate and heavy rainfall categories, indicating nearly unbiased forecasts. For thresholds above 100 mm d^{-1} , WRF_NJU tends to overpredict while the global models unanimously underpredict rainfall.

Further dividing 24 h rainfall into four periods of 6 h accumulated rainfall reveals the onset timing of the different heavy precipitation centers. WRF_NJU forecasts show good agreement with observations, reproducing the morning and afternoon peaks along the south coast, and the single early morning peak west of

Sichuan Basin and along the Yangtze River. The previously documented overprediction of coastal precipitation is found to occur mainly in the afternoon (14–20 LST) over the Nanling Mountains near south China coast, suggesting that the biggest challenge of quantitative precipitation forecasting is with convective precipitation. In comparison, the global models did much worse in reproducing diurnal variations. ECMWF performed best while JMA model showed the weakest diurnal variations. Most of the serious overprediction of the CMA model happened in the morning hours (08–14 LST).

Apart from the bulk characteristics, the WRF_NJU forecasts are further evaluated with respect to unique features of summer precipitation in China. In the monthly mean precipitation distributions, the WRF_NJU forecasts reproduce the south to north migration from June to July, followed by the southward retreat of the main precipitation band in August as in the observations. They also capture the large differences between 2013 and 2014 consistent with seasonal large-scale circulation differences.

The diurnal variations of precipitation are examined next. Time series of WRF_NJU forecast daily maximum and mean precipitation agree well with observations, except for the overprediction of maximum precipitation over a few days. In terms of the diurnal time series of domain averaged hourly rainfall, the WRF_NJU forecasts follow closely the observations, exhibiting a primary peak in late afternoon (17 LST) and a secondary peak in early morning (6 LST), although the magnitude of the afternoon peak is slightly overpredicted. Spatial distributions of daily peak hour show that the afternoon peak dominates most of China while the midnight peak appears in the Sichuan Basin and the early morning peak is prevalent along the Yangtze River at midlatitudes. The WRF_NJU forecasts reproduce the overall patterns well, except for some exaggeration of the extent of the morning peak regions.

Rain episodes during the summer months show mostly eastward and southward propagations, but episodes of westward and northward propagations associated with tropical cyclone activities are also found in the Hovmöller diagrams. Inland propagation of coastal precipitation in the morning is also evident near the south coast. The WRF_NJU forecasts are able to reproduce the onset timing, location, duration, and propagation direction of the main precipitation episodes during 2013–2014. The correlation coefficients of Hovmöller diagrams for latitudinal propagation between forecasts and observations are 0.83, 0.75, and 0.86 for June, July, and August, respectively, while those for longitudinal propagation are lower at 0.67, 0.57, and 0.56, respectively. Compared to latitudinal propagation that is usually under the influence of large scale circulations, longitudinal propagation is more difficult to predict as it mainly corresponds to the propagation of individual convective systems. The most prominent issue of overpredicting afternoon convective precipitation near south China coast requires further investigations, as do other smaller deficiencies.

Acknowledgments

This work was primarily supported by the National 973 Fundamental Research Program of China (grant 2013CB430103) and the National Science Foundation of China (grant 41405100). The work was also supported by the Foundation of China Meteorological Administration special (grant GYHY201506006). Comments of three anonymous reviewers helped improve our manuscript. The gridded data at reduced resolution including rain gauge observations and WRF forecasts are available at <https://pan.baidu.com/s/1dEBTKbv> (password: sxcd). For more detailed data, please contact us via e-mail.

References

- Baldauf, M., Seifert, A., Förstner, J., Majewski, D., Raschendorfer, M., & Reinhardt, T. (2011). Operational convective-scale numerical weather prediction with the COSMO model: Description and sensitivities. *Monthly Weather Review*, *139*(12), 3887–3905.
- Bao, X., Zhang, F., & Sun, J. (2011). Diurnal variations of warm-season precipitation east of the Tibetan Plateau over China. *Monthly Weather Review*, *139*(9), 2790–2810.
- Benjamin, S. G., Weygandt, S. S., Brown, J. M., Hu, M., Alexander, C. R., Smirnova, T. G., ... Manikin, G. S. (2016). A North American hourly assimilation and model forecast cycle: The rapid refresh. *Monthly Weather Review*, *144*(4), 1669–1694. <https://doi.org/10.1175/MWR-D-15-0242.1>
- Berenguer, M., Surcel, M., Zawadzki, I., Xue, M., & Kong, F. (2012). The diurnal cycle of precipitation from continental radar mosaics and numerical weather prediction models. Part II: Intercomparison between numerical models and with nowcasting. *Monthly Weather Review*, *140*, 2689–2705.
- Betts, A. K., & Jakob, C. (2002). Evaluation of the diurnal cycle of precipitation, surface thermodynamics, and surface fluxes in the ECMWF model using LBA data. *Journal of Geophysical Research*, *107*(D20), 8045. <https://doi.org/10.1029/2001JD000427>
- Bolin, B. (1956). An improved barotropic model and some aspects of using the balance equation for three-dimensional flow. 1. *Tellus*, *8*(1), 61–75.
- Bougeault, P., Toth, Z., Bishop, C., Brown, B., Burridge, D., Chen, D. H., ... Worley, S. (2010). The THORPEX interactive grand global ensemble. *Bulletin of the American Meteorological Society*, *91*(8), 1059–1072. <https://doi.org/10.1175/2010BAMS2853.1>
- Brown, B. G., Gotway, J. H., Bullock, R., Gilleland, E., & Ahijevych, D. (2009). The Model Evaluation Tools (MET): Community tools for forecast evaluation. In *25th Conference on International Interactive Information and Processing Systems (IIPS) for Meteorology, Oceanography, and Hydrology*, p. Paper 9A.6.
- Browning, K. A., Morcrette, C. J., Nicol, J., Blyth, A. M., Bennett, L. J., Brooks, B. J., ... Watson, R. J. (2007). The convective storm initiation project. *Bulletin of the American Meteorological Society*, *88*(12), 1939–1955. <https://doi.org/10.1175/BAMS-88-12-1939>
- Bryan, G. H., & Morrison, H. (2011). Sensitivity of a simulated squall line to horizontal resolution and parameterization of microphysics. *Monthly Weather Review*, *140*(1), 202–225.
- Burpee, R. W., & Lahiff, L. N. (1984). Area-average rainfall variations on sea-breeze days in South Florida. *Monthly Weather Review*, *112*(3), 520–534.

- Candille, G., Cote, C., Houtekamer, P. L., & Pellerin, G. (2007). Verification of an ensemble prediction system against observations. *Monthly Weather Review*, 135(7), 2688–2699.
- Carbone, R. E., Tuttle, J. D., Ahijevych, D. A., & Trier, S. B. (2002). Inferences of predictability associated with warm season precipitation episodes. *Journal of the Atmospheric Sciences*, 59(13), 2033–2056.
- Chen, G., Sha, W., & Iwasaki, T. (2009). Diurnal variation of precipitation over southeastern China: Spatial distribution and its seasonality. *Journal of Geophysical Research*, 114, D13103. <https://doi.org/10.1029/2008JD011103>
- Chen, H., Yu, R., Li, J., Yuan, W., & Zhou, T. (2010). Why nocturnal long-duration rainfall presents an eastward-delayed diurnal phase of rainfall down the Yangtze River Valley. *Journal of Climate*, 23(4), 905–917.
- Chen, X., Zhao, K., & Xue, M. (2014). Spatial and temporal characteristics of warm season convection over Pearl River Delta region, China, based on 3 years of operational radar data. *Journal of Geophysical Research: Atmospheres*, 119, 12,447–12,465. <https://doi.org/10.1002/2014JD021965>
- Chen, X., Zhao, K., Xue, M., Zhou, B., Huang, X., & Xu, W. (2015). Radar-observed diurnal cycle and propagation of convection over the Pearl River Delta during Mei-Yu season. *Journal of Geophysical Research: Atmospheres*, 120, 12,557–12,575. <https://doi.org/10.1002/2015JD023872>
- Clark, A. J., Gallus, W. A. Jr., Xue, M., & Kong, F. (2009). A comparison of precipitation forecast skill between small convection-permitting and large convection-parameterizing ensembles. *Weather and Forecasting*, 24, 1121–1140.
- Clark, A. J., Gallus, W. A., & Chen, T. C. (2007). Comparison of the diurnal precipitation cycle in convection-resolving and non-convection-resolving mesoscale models. *Monthly Weather Review*, 135, 3456–3473.
- China Meteorological Administration (2016). Yearbook of meteorological disasters in China (in Chinese) (Rep., pp. 2–3).
- Collins, W. D., Rasch, P. J., Boville, B. A., Hack, J. J., Mccaa, J. R., Williamson, D. L., ... Dai, Y. (2004). Description of the NCAR Community Atmosphere Model (CAM 3.0) (NCAR Technical Note NCAR/TN-464+STR, pp. 226). Boulder, CO: National Center for Atmospheric Research. <https://doi.org/10.5065/D63N21CH>
- Dai, A. (2001). Global precipitation and thunderstorm frequencies. Part II: Diurnal variations. *Journal of Climate*, 14(6), 1112.
- Dai, A. (2006). Precipitation characteristics in eighteen coupled climate models. *Journal of Climate*, 19(18), 4605–4630.
- Davis, C. A., Manning, K. W., Carbone, R. E., Trier, S. B., & Tuttle, J. D. (2003). Coherence of warm-season continental rainfall in numerical weather prediction models. *Monthly Weather Review*, 131(11), 2667–2679.
- Ding, Y. (1992). Summer monsoon rainfalls in China. *Journal of the Meteorological Society of Japan Series II*, 70(1B), 373–396.
- Ding, Y. (2015). On the study of the unprecedented heavy rainfall in Henan Province during 4–8 August 1975: Review and assessment (in Chinese). *Acta Meteorologica Sinica*, 73(3), 411–424.
- Ding, Y., & Chan, J. C. L. (2005). The East Asian summer monsoon: An overview. *Meteorology and Atmospheric Physics*, 89(1), 117–142.
- Fowle, M. A., & Roebber, P. J. (2003). Short-range (0–48 h) numerical prediction of convective occurrence, mode, and location. *Weather and Forecasting*, 18(5), 782–794.
- Gandin, L. S., & Murphy, A. H. (1992). Equitable skill scores for categorical forecasts. *Monthly Weather Review*, 120(2), 361–370.
- Gilleland, E. (2013). Testing competing precipitation forecasts accurately and efficiently: The spatial prediction comparison test. *Monthly Weather Review*, 141(1), 340–355.
- Hamill, T. M. (1999). Hypothesis tests for evaluating numerical precipitation forecasts. *Weather and Forecasting*, 14(2), 155–167.
- Huang, A., Zhao, Y., Zhou, Y., Yang, B., Zhang, L., Dong, X., ... Wu, Y. (2016). Evaluation of multisatellite precipitation products by use of ground-based data over China. *Journal of Geophysical Research: Atmospheres*, 121, 10,654–10,675. <https://doi.org/10.1002/2016JD025456>
- Kidd, C., Dawkins, E., & Huffman, G. (2013). Comparison of precipitation derived from the ECMWF operational forecast model and satellite precipitation datasets. *Journal of Hydrometeorology*, 14(5), 1463–1482.
- Lau, K.-M., & Li, M.-T. (1984). The monsoon of East Asia and its global associations—A survey. *Bulletin of the American Meteorological Society*, 65(2), 114–125.
- Lin, J., & Yang, G. (2014). Spatio-temporal characteristics of rainstorm in China during 1981–2010 (in Chinese). *Meteorological Monthly*, 40(7), 816–826.
- Liu, C., Moncrieff, M. W., Tuttle, J. D., & Carbone, R. E. (2006). Explicit and parameterized episodes of warm-season precipitation over the continental United States. *Advances in Atmospheric Sciences*, 23(1), 91–105.
- Luo, Y. L., Zhang, R., Wan, Q., Wang, B., Wong, W. K., Hu, Z., ... Xiao, Y. (2017). The Southern China Monsoon Rainfall Experiment (Scmrex). *Bulletin of the American Meteorological Society*, 98(5), 999–1013. <https://doi.org/10.1175/BAMS-D-15-00235.1>
- Morrison, H., Curry, J. A., & Khvorostyanov, V. I. (2005). A new double-moment microphysics parameterization for application in cloud and climate models. Part I: Description. *Journal of the Atmospheric Sciences*, 62, 1665–1677.
- Neale, R. B., Gettelman, A., Park, S., Conley, A. J., Kinnison, D., Marsh, D., ... Rasch, P. J. (2010). Description of the NCAR Community Atmosphere Model (CAM 5.0) (NCAR Tech. Note NCAR/TN-4861STR, pp. 238). Boulder, CO: National Center for Atmospheric Research.
- Oki, T., & Musiaka, K. (1994). Seasonal change of the diurnal cycle of precipitation over Japan and Malaysia. *Journal of Applied Meteorology*, 33(12), 1445–1463.
- Pan, Y., Zhu, K., Xue, M., Wang, X., Hu, M., Benjamin, S. G., ... Whitaker, J. S. (2014). A GSI-based coupled EnSRF–En3DVar hybrid data assimilation system for the operational rapid refresh model: Tests at a reduced resolution. *Monthly Weather Review*, 142(10), 3756–3780.
- Pleim, J. E. (2006). A simple, efficient solution of flux–profile relationships in the atmospheric surface layer. *Journal of Applied Meteorology and Climatology*, 45(2), 341–347.
- Pleim, J. E. (2007). A combined local and nonlocal closure model for the atmospheric boundary layer. Part I: Model description and testing. *Journal of Applied Meteorology and Climatology*, 46(9), 1383–1395.
- Saito, K., Fujita, T., Yamada, Y., Ishida, J. i., Kumagai, Y., Aranami, K., ... Yamazaki, Y. (2006). The operational JMA nonhydrostatic mesoscale model. *Monthly Weather Review*, 134(4), 1266–1298. <https://doi.org/10.1175/MWR3120.1>
- Schwartz, C., Kain, J., Weiss, S., Xue, M., Bright, D., Kong, F., ... Coniglio, M. (2009). Next-day convection-allowing WRF model guidance: A second look at 2 vs. 4 km grid spacing. *Monthly Weather Review*, 137, 3351–3372.
- Seity, Y., Brousseau, P., Malardel, S., Hello, G., Bénard, P., Bouttier, F., ... Masson, V. (2011). The AROME-France Convective-Scale Operational Model. *Monthly Weather Review*, 139(3), 976–991.
- Shuman, F. G. (1957). Numerical methods in weather prediction: I. The balance equation. *Monthly Weather Review*, 85(10), 329–332.
- Skamarock, W. C., Klemp, J. B., Dudhia, J., Gill, D. O., Barker, D. M., Wang, W., & Powers, J. D. (2005). A description of the Advanced Research WRF version 2 (Rep., 88 pp.). NCAR.
- Smith, T. L., Benjamin, S. G., Brown, J. M., Weygandt, S. S., Smirnova, T., & Schwartz, B. (2008). Convection forecasts from the hourly updated, 3-km High Resolution Rapid Refresh (HRRR) model. In *24th Conference on Severe Local Storms* (Rep. 11.21 pp.). Savannah, GA: American Meteorological Society.

- Staniforth, A., & Wood, N. (2008). Aspects of the dynamical core of a nonhydrostatic, deep-atmosphere, unified weather and climate-prediction model. *Journal of Computational Physics*, 227(7), 3445–3464.
- Sun, J., Xue, M., Wilson, J. W., Zawadzki, I., Ballard, S. P., Onvlee-Hooimeyer, J., ... Pinto, J. (2013). Use of NWP for nowcasting convective precipitation: Recent progress and challenges. *Bulletin of the American Meteorological Society*, 95(3), 409–426.
- Sun, J., & Zhang, F. (2012). Impacts of mountain–plains solenoid on diurnal variations of rainfalls along the Mei-Yu Front over the East China Plains. *Monthly Weather Review*, 140(2), 379–397.
- Swinbank, R., Kyouda, M., Buchanan, P., Froude, L., Hamill, T. M., Hewson, T. D., ... Yamaguchi, M. (2016). The TIGGE project and its achievements. *Bulletin of the American Meteorological Society*, 97(1), 49–67. <https://doi.org/10.1175/BAMS-D-13-00191.1>
- Tang, Y., Lean, H. W., & Bornemann, J. (2013). The benefits of the Met Office variable resolution NWP model for forecasting convection. *Meteorological Applications*, 20(4), 417–426.
- Wang, Q., Xue, M., & Tan, Z. (2016). Convective initiation by topographically induced convergence forcing over the Dabie Mountains on 24 June 2010. *Advances in Atmospheric Science*, 33(10), 1120–1136.
- Weisman, M. L., Davis, C., Wang, W., Manning, K. W., & Klemp, J. B. (2008). Experiences with 0–36-h explicit convective forecasts with the WRF-ARW model. *Weather and Forecasting*, 23(3), 407–437.
- Wen, Y. R., Xue, L., Li, Y., Wei, N., & Lu, A. M. (2015). Interaction between Typhoon Vicente (1208) and the western Pacific subtropical high during the Beijing extreme rainfall of 21 July 2012. *Journal of Meteorological Research*, 29(2), 293–304.
- Xue, M. (2016). Preface to the special issue on the “Observation, prediction and analysis of severe convection of China” (OPACC) National “973” Projec. *Advances in Atmospheric Sciences*, 33(10), 1099–1101.
- Xue, M., Kong, F., Thomas, K. W., Gao, J., Wang, Y., Brewster, K., ... Du, J. (2007). CAPS realtime storm-scale ensemble and highresolution forecasts as part of the NOAA Hazardous Weather Testbed 2007 spring experiment. In *22nd Conf. Wea. Anal. Forecasting/18th Conf. Num. Wea. Pred.* (CDROM 3B.1). Salt Lake City, Utah: American Meteorological Society.
- Yu, R., Li, J., & Chen, H. (2008). Diurnal variation of surface wind over central eastern China. *Climate Dynamics*, 33(7), 1089–1097.
- Yu, R., Li, J., Chen, H., & Yuan, W. (2014). Progress in studies of the precipitation diurnal variation over contiguous China (in Chinese). *Acta Meteorologica Sinica*, 72(5), 948–968.
- Yu, R., Xu, Y., Zhou, T., & Li, J. (2007). Relation between rainfall duration and diurnal variation in the warm season precipitation over central eastern China. *Geophysical Research Letters*, 34, L13703. <https://doi.org/10.1029/2007GL030315>
- Yu, R., Zhou, T., Xiong, A., Zhu, Y., & Li, J. (2007). Diurnal variations of summer precipitation over contiguous China. *Geophysical Research Letters*, 34, L01704. <https://doi.org/10.1029/2006GL028129>
- Yuan, W., Yu, R., Zhang, M., Lin, W., Chen, H., & Li, J. (2012). Regimes of diurnal variation of summer rainfall over subtropical East Asia. *Journal of Climate*, 25(9), 3307–3320.
- Yuan, W., Yu, R., Zhang, M., Lin, W., Li, J., & Fu, Y. (2013). Diurnal cycle of summer precipitation over subtropical East Asia in CAM5. *Journal of Climate*, 26(10), 3159–3172.
- Zheng, Y., Xue, M., Li, B., Chen, J., & Tao, Z. (2016). Spatial characteristics of extreme rainfall over China with hourly through 24-hour accumulation periods based on national-level hourly rain gauge data. *Advances in Atmospheric Sciences*, 33(11), 1218–1232.
- Zhou, T., Yu, R., Chen, H., Dai, A., & Pan, Y. (2008). Summer precipitation frequency, intensity, and diurnal cycle over China: A comparison of satellite data with rain gauge observations. *Journal of Climate*, 21(16), 3997–4010.
- Zhou, T.-J., & Yu, R.-C. (2005). Atmospheric water vapor transport associated with typical anomalous summer rainfall patterns in China. *Journal of Geophysical Research*, 110, D08104. <https://doi.org/10.1029/2004JD005413>
- Zhu, K., & Xue, M. (2016). Evaluation of WRF-based convection-permitting multi-physics ensemble forecasts over China for an extreme rainfall event on 21 July 2012 in Beijing. *Advances in Atmospheric Sciences*, 33(11), 1240–1258.